Research Square

Preprints are preliminary reports that have not undergone peer review.
They should not be considered conclusive, used to inform clinical practice,
or referenced by the media as validated information.

Preparation-dependent pyrolysis kinetics of rosehip seed, skin, and whole fruit: Multirate TG–DTG analysis and DAEM adequacy assessment

Ahsanullah Soomro

ahsanullah.soomro@yildiz.edu.tr

Yildiz Technical University

Anıl Tevfik Koçer

Yildiz Technical University

Iqra panhwar

Yildiz Technical University

Zafar Ali Siyal

Quaid-e-Awam University of Engineering, Science and Technology (QUEST)

Mahdi Hassan

Quaid-e-Awam University of Engineering, Science and Technology (QUEST)

Hamid Rehman

Yildiz Technical University

Tasawar Ali Chandio

Yildiz Technical University

Didem Balkanlı

Yildiz Technical University

Research Article

Keywords: Rosehip, Thermogravimetric analysis, Derivative thermogravimetry, Isoconversional kinetics, Analytical-support screening, Distributed activation energy model

Posted Date: August 24th, 2026

DOI: https://doi.org/10.21203/rs.3.rs-10532516/v1

License: This work is licensed under a Creative Commons Attribution 4.0 International License.
Read Full License

Additional Declarations: No competing interests reported.

Preparation-dependent pyrolysis kinetics of rosehip seed, skin, and whole fruit: Multirate TG–DTG analysis and DAEM adequacy assessment

Ahsanullah Soomro[1,2,*] Anıl Tevfik Koçer[1,3], Iqra panhwar[4], Zafar Ali Siyal[2], Mahdi Hassan[2,4] Hamid Rehman[4] Tasawar Ali Chandio[5] and Didem Balkanlı[1].

[1]Department of Bioengineering, Yildiz Technical University, 34220, Istanbul, Turkey

[2] Environment Engineering Department, Quaid-e-Awam University of Engineering, Science and Technology (QUEST), Nawabshah, Sindh, Pakistan

[3]Health Biotechnology Joint Research and Application Center of Excellence, 34220, Istanbul, Turkey

[4]Department of Environment Engineering, Yildiz Technical University, 34220, Istanbul, Turkey

[5]Department of Metallurgical and Materials Engineering, Glass Research and Development Laboratory, 34220, Istanbul, Turkey

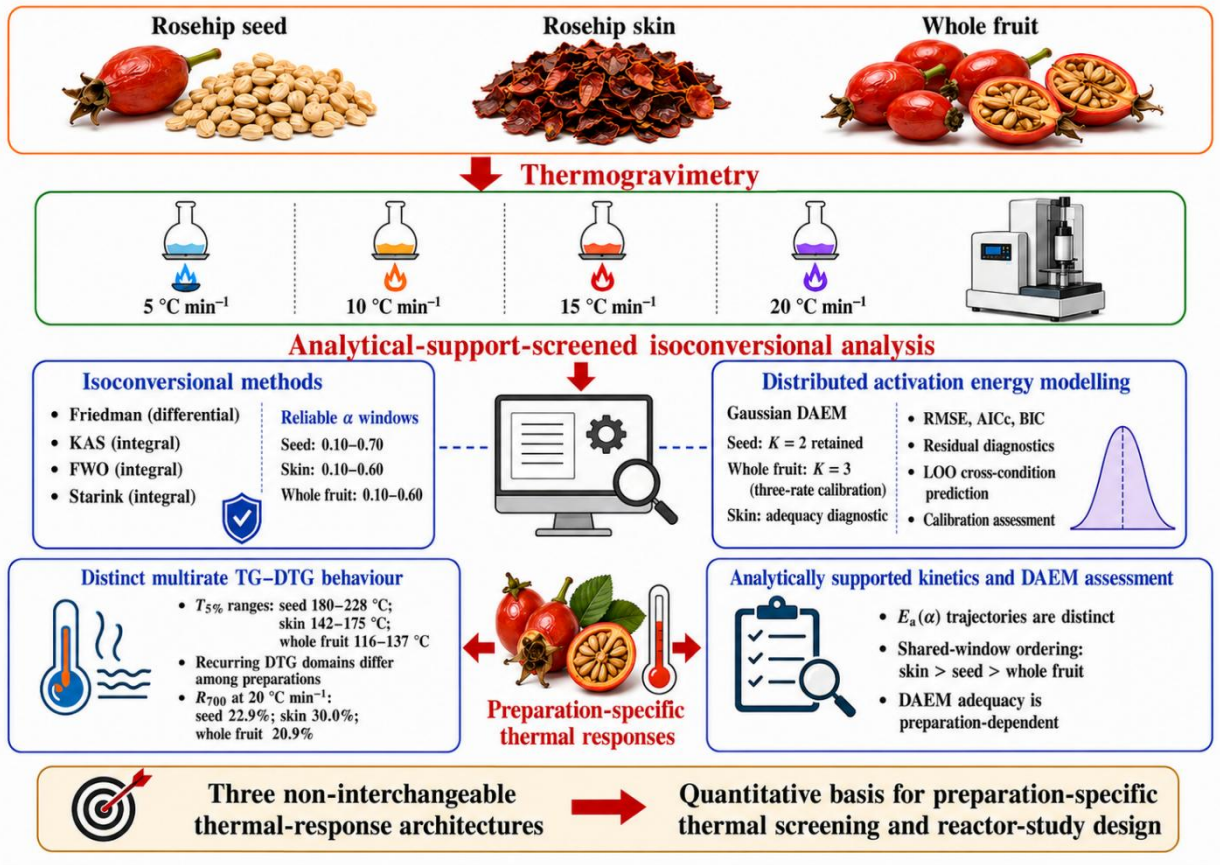
*Corresponding author: ahsanullah.soomro@yildiz.edu.tr

Abstract

Rosehip seed, skin, and whole-fruit preparations from a matched batch were compared under nitrogen at heating rates of 5, 10, 15, and 20 °C min^{-1} to determine whether they shared a common thermal response or required preparation-specific interpretation. The analysis combined measured TG–DTG profiles, recurring thermal domains, analytically screened apparent activation-energy trajectories from the Friedman, Kissinger–Akahira–Sunose, Flynn–Wall–Ozawa, and Starink methods, and Gaussian distributed activation energy modelling. Seed showed the latest low-conversion response and a concentrated higher-temperature conversion zone, with T_5% = 180.3–228.0 °C, a recurring domain at 332–360 °C, and integral-method $E_a(\alpha)$ increasing from 99.25 to 147.16 kJ mol^{-1} over α = 0.10–0.70. Skin converted earlier through recurring domains at 173–223 and 310–336 °C, while $E_a(\alpha)$ decreased from 277.22 to 152.21 kJ mol^{-1} over α = 0.40–0.60, indicating the strongest conversion dependence. Whole fruit showed the earliest T_5% values (116.0–136.9 °C) and recurring domains at 174–225 and 333–352 °C; $E_a(\alpha)$ increased from 115.02 to 139.04 kJ mol^{-1} over α = 0.30–0.60. Endpoint testing at 600–700 °C preserved trajectory directions and shared-window ordering, although skin showed the greatest magnitude sensitivity. The seed K = 2 model provided a compact description with partial cross-condition transfer, skin was represented most reliably by measured TG–DTG and isoconversional results, and the whole-fruit K = 3 model fitted the calibration curves without independent predictive validation. The findings establish three non-interchangeable thermal-response architectures and support preparation-specific thermal screening and reactor-study design.

Keywords: Rosehip; Thermogravimetric analysis; Derivative thermogravimetry; Isoconversional kinetics; Analytical-support screening; Distributed activation energy model

Graphical Abstract



Nomenclature

Symbol / term	Definition
Abbreviations and model-quality statistics	
TGA	Thermogravimetric analysis.
TG	Thermogravimetric mass signal, reported as normalized mass remaining.
DTG$_t$(T)	Positive time-based mass-loss rate, $-d[100w(T)]/dt$.
DTG$_T$(T)	Positive temperature-based mass-loss rate, $-d[100w(T)]/dT$.
DTG$_{t,max}$	Maximum positive time-based DTG value on a curve.
KAS	Kissinger–Akahira–Sunose integral isoconversional method.
FWO	Flynn–Wall–Ozawa integral isoconversional method.
DAEM	Distributed activation energy model.
LOO	Leave-one-heating-rate-out cross-condition assessment.
RMSE	Root-mean-square error.
RSS	Residual sum of squares.
SSE	Sum of squared errors; used synonymously with RSS where explicitly stated.
AICc	Finite-sample corrected Akaike information criterion; used for relative ranking within the tested candidate set.

BIC	Bayesian information criterion; used for relative ranking within the tested candidate set.
R^2	Coefficient of determination of a fitted linear relation.
SE(E_a)	Regression-derived standard error of apparent activation energy.
CV	Coefficient of variation used for descriptive cross-method comparison.
FWHM	Full width at half maximum of a fitted Gaussian component.
r_1	Lag-1 residual autocorrelation coefficient used to diagnose serial residual structure.
p_{runs}	Runs-test probability used to assess non-random residual ordering.
TG, stage-wise, and characteristic-temperature notation	
t	Time.
T	Temperature.
β	Programmed linear heating rate, dT/dt.
β_{max}/β_{min}	Ratio of the maximum to minimum programmed heating rate.
$m(T)$	Instantaneous sample mass at temperature T.
m_0	First valid sample mass of the corresponding TG run.
$w(T)$	Dimensionless mass fraction, $w(T)=m(T)/m_0$.
$W(T)$	Cumulative percentage mass loss, $W(T)=100[1-w(T)]$.
R_{700}	Normalized mass remaining at 700 °C when the heating-rate qualifier is omitted; the applicable rate is specified by context.
$R_{700,\beta}$	Rate-specific normalized mass remaining at 700 °C; it is the endpoint used in the operational 150–700 °C conversion coordinate.
$R_{700,20}$	Normalized mass remaining at 700 °C for the 20 °C min^{-1} stage-resolved and integrated comparisons.
ΔW_{I}	Mass loss in Stage I, from the first valid temperature to 150 °C.
ΔW_{II}	Mass loss in Stage II, 150–400 °C.
ΔW_{III}	Mass loss in Stage III, 400–700 °C.
$T_{5\%}$, $T_{10\%}$, $T_{50\%}$	Temperatures at cumulative losses of 5%, 10%, and 50% of the initial sample mass, respectively.
T_C	Interpolated characteristic or fixed-conversion temperature obtained by first-bracket linear interpolation.
T_1, T_2	Temperatures bracketing an interpolation target.
P_1, P_2	Property values corresponding to T_1 and T_2 in the interpolation relation.
P_S	Target property value in the interpolation relation.
Stage I	Fixed comparative interval from the first valid temperature to 150 °C mechanism-specific.
Stage II	Fixed comparative interval from 150 to 400 °C
Stage III	Fixed comparative interval from 400 to 700 °C
Isoconversional and peak-shift notation	
$\alpha(T)$	Fractional conversion defined over the operational 150–700 °C interval.
m_{150}	Interpolated sample mass at 150 °C used as the initial mass for α.
m_{700}	Interpolated sample mass at 700 °C used as the final mass for α.
T_α	Temperature corresponding to a specified conversion α.
$T_{\alpha,i}$	Temperature at conversion α for heating-rate experiment index i.
β_i	Programmed heating rate for isoconversional experiment index i.

***i* (isoconversional)**	Heating-rate experiment index in fixed-conversion regressions.
$d\alpha/dt$	Time-based conversion rate used in the Friedman method.
$d\alpha/dT$	Temperature-based conversion rate.
$E_a(\alpha) \equiv E_\alpha$	Conversion-dependent apparent activation energy; E_α is the fixed-conversion notation used in Eqs. (2a)–(2d).
A_α	Apparent pre-exponential factor at fixed conversion α; it is absorbed into the regression intercept and is not interpreted separately.
$f(\alpha)$	Differential reaction-model function appearing in the Friedman expression.
$g(\alpha)$	Integral reaction-model function appearing in integral isoconversional derivations.
$C_{\alpha,\mathrm{KAS}}$	Fixed-conversion regression intercept in the KAS relation.
$C_{\alpha,\mathrm{FWO}}$	Fixed-conversion regression intercept in the FWO relation.
$C_{\alpha,\mathrm{Starink}}$	Fixed-conversion regression intercept in the Starink relation.
s_α	Slope of the fixed-conversion linear regression at α; s_α is used rather than m_α to avoid confusion with sample mass.
R	Universal gas constant.
T_p	Tracked DTG peak temperature used in the Kissinger diagnostic.
$E_{\mathrm{K,p}}$	Apparent peak-based activation energy obtained from the Kissinger regression.
C_{K}	Regression intercept in the Kissinger relation.
Recurring DTG-domain descriptors	
$T_{p,1}$; $T_{p,2}$	Peak temperatures of the lower- and higher-temperature recurring DTG domains, respectively.
$H_{p,1}$; $H_{p,2}$	Raw DTG heights at $T_{p,1}$ and $T_{p,2}$, respectively.
R_{H}	Relative peak-height ratio, $R_{\mathrm{H}}=H_{p,2}/H_{p,1}$.
ΔT_p	Inter-domain peak separation, $\Delta T_p=T_{p,2}-T_{p,1}$.
ΔDTG	Within-curve DTG range used in the peak-prominence eligibility rule.
c_β	Heating-rate-scaled prominence coefficient in the peak-eligibility rule; the adopted value is 0.02 % °C^{-1}.
Conditional Gaussian DTG-decomposition notation	
$y(T)$	Fitted baseline-corrected DTG signal represented by the Gaussian sum in Eq. (5).
$G_j(T)$	Contribution of Gaussian component j to the fitted baseline-corrected DTG signal.
$A_{\mathrm{G,j}}$	Integrated area of Gaussian component j; subscript G distinguishes this quantity from the DAEM pre-exponential factor $A_{r,j}$.
$\mu_{\mathrm{T,j}}$	Centre temperature of Gaussian component j.
$\sigma_{\mathrm{T,j}}$	Temperature-domain standard deviation (width parameter) of Gaussian component j.
FWHM_j	Full width at half maximum of Gaussian component j.
K_{G}	Number of Gaussian components in the conditional DTG decomposition.
y_i; $\hat{y}_i$	Observed and fitted baseline-corrected DTG values at observation i, respectively.
e_i	Observed-minus-fitted DTG residual, $e_i=y_i-\hat{y}_i$.
n	Number of observations used in a fitted Gaussian candidate.
k	Number of fitted parameters used in AICc and BIC.

Distributed-reactivity (Gaussian DAEM) notation	
r	Feedstock index, $r \in$ {rosehip seed, rosehip skin, whole-fruit rosehip}.
j	Formal DAEM reactivity-domain index.
i **(DAEM)**	Temperature-observation index within a TG curve.
K	Number of formal reactivity domains in the candidate DAEM.
T_0	Initial temperature of the distributed-reactivity model interval, 423.15 K (150 °C).
$\mathscr{B}$	Complete experimental heating-rate set, $\mathscr{B}=\{5,10,15,20\}$.
$\mathscr{B}_{\mathrm{fit}}$	Subset of heating rates used for parameter estimation.
$\lvert\mathscr{B}_{\mathrm{fit}}\rvert$	Number of heating rates included in a fit.
β_h	Heating rate withheld from a seed or skin LOO calibration.
$\mathscr{B}\backslash\{\beta_h\}$	Calibration-rate set after exclusion of β_h; equivalently, $\{\beta \in \mathscr{B}: \beta \neq \beta_h\}$.
$\theta_{r,K}$	Parameter vector for feedstock r and a K-domain model: $\{A_{r,j}, \mu_{\mathrm{E,r,j}}, \sigma_{\mathrm{E,r,j}}, c_{r,j}\}$, $j=1,\ldots,K$.
$\hat{\theta}_{r,K}$	Optimized parameter vector for feedstock r and the K-domain model.
$\hat{\theta}_{r,K}^{(-\beta_h)}$	Optimized parameter vector estimated without the curve at β_h.
$\Theta_{r,K}$	Feasible parameter space defined by imposed bounds and ordering constraints.
$A_{r,j}$	Pre-exponential factor of DAEM domain j for feedstock r.
$\mu_{\mathrm{E,r,j}}$	Mean activation energy of DAEM domain j for feedstock r.
$\sigma_{\mathrm{E,r,j}}$	Activation-energy distribution width of DAEM domain j for feedstock r.
$c_{r,j}$	Fitted post-150 °C mass-loss capacity of formal domain j.
E	Activation energy integrated over the DAEM distribution.
$D_{r,j}(E)$	Normalized Gaussian activation-energy density of DAEM domain j.
$\alpha_{r,j}(T,E;\beta)$	Reacted fraction at activation energy E for domain j of feedstock r.
$\bar{\alpha}_{r,j}(T,\beta)$	Distribution-averaged reacted fraction of DAEM domain j.
$m_{r,\beta}(T)$	DAEM-predicted active-interval normalized mass in Eq. (9).
$m_{r,\beta}^{\mathrm{obs}}(T_i)$	Observed active-interval normalized mass at observation temperature T_i.
$m_{r,\beta}(T_i;\theta_{r,K})$	Model-predicted active-interval normalized mass used in the fitting objective.
$J_{r,K}(\theta_{r,K})$	Equal-heating-rate least-squares objective for feedstock r and the K-domain model.
$J_{r,K}^{(-\beta_h)}(\theta_{r,K})$	LOO calibration objective evaluated after withholding the curve at β_h.
$N_{r,\beta}$	Number of observations for feedstock r at heating rate β.
T_i	Temperature of observation i.
$\mathrm{RMSE}_{r,K}^{\mathrm{pred},(-\beta_h)}$	Prediction RMSE for the curve withheld at β_h.

1. Introduction

The increasing generation of fruit-processing residues has intensified interest in thermochemical routes that recover energy and carbon-rich solids while reducing disposal burdens [1]. Pyrolysis converts biomass in an oxygen-limited environment into char, condensable vapours, and permanent gases and constitutes the devolatilization stage underlying gasification and combustion [2]. Thermogravimetric analysis (TGA), together with derivative

thermogravimetry (DTG), provides a controlled multirate basis for resolving mass-loss intervals and evaluating apparent kinetics under conditions designed to minimize heat- and mass-transfer limitation [3,4]. Accordingly, TG–DTG serves as a comparative and kinetic-screening platform that can guide subsequent reactor-scale investigation [2,4].

Lignocellulosic biomass exhibits overlapping thermal responses arising from its heterogeneous structure. Hemicellulose generally contributes earlier conversion, cellulose produces a comparatively sharp dominant event, and lignin decomposes over a broader temperature range with greater solid retention [5,6]. The resulting TG–DTG profile therefore reflects superposed pseudo-component reactions rather than a single kinetic event [7,8]. Selected biomass-fuel mixtures can display approximately summative behaviour [9], whereas interactions among components and their primary products can shift product formation away from weighted expectations [10]. Accordingly, recurring DTG maxima and shoulders are treated here as operational thermal domains. This approach allows the architecture of each response to be compared without assigning individual domains to specific biochemical constituents in the absence of independent compositional or evolved-product evidence.

Rosehip processing yields distinct materials, including seeds, pulp or pomace, husk, and residues remaining after seed-oil recovery. Martín-Ramos et al. [11] reported distinct thermal responses for *Rosa rubiginosa* seeds, pulp, leaves, and seed oil and identified the seeds, pulp, and oil as potential biomass feedstocks. Subsequent studies investigated exhausted rosehip seed waste through multirate TGA, peak deconvolution, kinetic modelling, and slow-pyrolysis product analysis [12]; pectin-extracted husk residue through multirate TGA and fixed-bed slow pyrolysis [13]; designed seed-waste–husk-waste blends through co-pyrolysis followed by CO_2 gasification of the resulting biochars [14] ; rosehip seed waste through fast pyrolysis in a bubbling fluidized-bed reactor [15]; and rosehip seeds, pomace, and designed seed–pomace blends through fuel-property characterization, TG–DTA, and catalytic and non-catalytic Py–GC–MS [16]. Collectively, these studies establish the thermochemical relevance of rosehip residues, but they do not resolve whether seed, skin, and whole fruit from the same batch retain a common thermal response or require preparation-specific interpretation under an identical multirate protocol.

A second issue concerns kinetic interpretation. A single peak-based or global activation-energy value can conceal conversion-dependent changes in the effective reacting population [17,18]. Multirate isoconversional methods estimate the effective apparent activation energy as a function of conversion, $E_a(\alpha)$, without imposing one global reaction model over the complete conversion range [19,20]. The reliability of fixed-conversion estimates nevertheless depends on temperature-data processing, heating-program consistency, regression behaviour, and

experimental uncertainty [19,21,22]. The present work therefore applies study-defined analytical-support screening based on temperature ordering, regression behaviour, inter-method consistency, profile continuity, and TG–DTG correspondence. The resulting classes rank the analytical support of conversion levels within the four-rate dataset.

Distributed-reactivity models provide an additional means of representing the broad reactivity spectrum of biomass decomposition, but the lowest calibration error does not necessarily identify the most scientifically useful model. Kinetic compensation and parameter non-identifiability can allow materially different parameter combinations to reproduce the same TG curves. Várhegyi et al. [23] treated prediction tests as an essential component of distributed-activation-energy-model verification, while Soria-Verdugo et al. [21] showed that the number of heating-rate curves and the treatment of measurement uncertainty influence DAEM-derived activation energies and pre-exponential factors. The present analysis therefore distinguishes reduced-order descriptive performance, calibration without an independent prediction test, and performance supported by withheld-rate prediction. Fitted Gaussian distributions are interpreted as empirical reactivity modes rather than constituent identities.

The central question of this study is whether rosehip seed, an operationally defined skin fraction, and whole-fruit material can be represented by a common thermal and kinetic response or require preparation-specific interpretation. To address this question, all three preparations from a matched batch were evaluated under an identical non-isothermal multirate thermogravimetric protocol using characteristic mass-loss temperatures, fixed-interval mass losses, recurring DTG domains, and conversion-dependent apparent activation-energy profiles, $E_a(\alpha)$, obtained by the Friedman, Kissinger–Akahira–Sunose, Flynn–Wall–Ozawa, and Starink methods. Whole-fruit behaviour was measured directly rather than reconstructed from the separated fractions. Gaussian distributed activation energy models were subsequently assessed using calibration error, parameter behaviour, residual structure, derivative-shape fidelity, and cross-rate performance to distinguish descriptive agreement from transferable predictive representation. To the best of our knowledge, this is the first matched-batch comparison of rosehip seed, an operationally defined skin fraction, and directly measured whole-fruit material that integrates multirate TG–DTG architecture, analytical-support-screened $E_a(\alpha)$ trajectories, and distributed-reactivity model-adequacy testing within a single evidence framework. This approach determines whether the preparations are thermally interchangeable and demonstrates that low calibration error alone does not establish a stable, transferable, or derivative-faithful kinetic representation. The resulting preparation-specific interpretation provides a quantitative basis for thermal screening and for designing subsequent reactor studies around the distinct conversion behaviour of each rosehip preparation.

2. Materials and methods

2.1. Rosehip feedstock selection and preparation

Rosehip fruits obtained from a local market were dried before processing through two routes (Fig. 1). For anatomical separation, dried fruits were manually divided into seed and an operationally defined outer skin/peel fraction, after which each fraction was ground independently using the same archived preparation procedure. For the unfractionated preparation, dried fruits were ground directly without separation. Whole-fruit powder therefore retained naturally co-occurring seed, skin/peel, pulp/flesh and other tissues and was not produced by recombining isolated fractions.

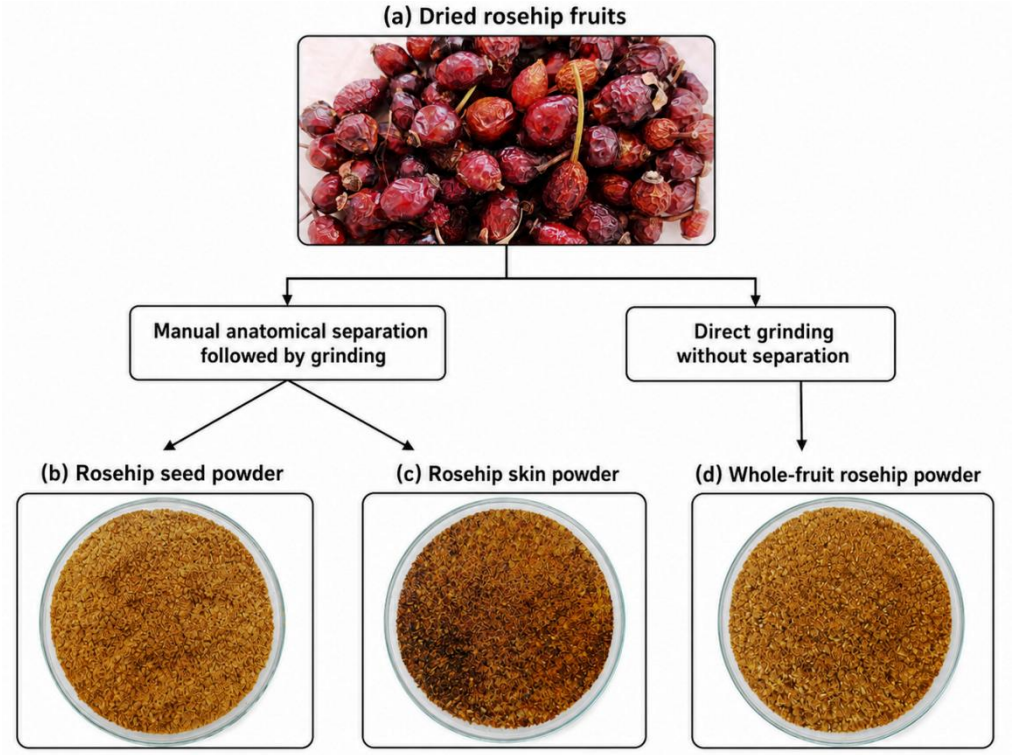


Fig. 1. Preparation routes for rosehip seed, skin and whole-fruit powders. Dried fruits were either separated into seed and skin before grinding or ground directly to obtain the whole-fruit preparation.

2.2. Thermogravimetric analysis

Dynamic non-isothermal thermogravimetric measurements were performed using an SDT Q600 simultaneous thermal analyzer (TA Instruments, New Castle, DE, USA). Approximately 5 mg of dried, ground feedstock was placed in an alumina crucible and heated under nitrogen (50 mL min^{-1}) at β = 5, 10, 15, and 20 °C min^{-1}. The analytical temperature range was restricted to ambient temperature–700 °C. Although the exported raw records contained additional valid points up to 781–788 °C, all reported calculations and model fits excluded data above 700 °C (Supplementary Table S8). Crucible type, purge flow, analytical endpoint, and acquisition procedure were held constant.

.

2.3. TG–DTG data processing and characteristic parameters

TG records were normalized to the first valid temperature–mass datum. Initial mass gains were retained as run-level quality-control flags and were not interpreted as conversion; the associated start-up balance/buoyancy behaviour is summarized in Supplementary Table S8 [8]. Cumulative mass loss was calculated using Eq. (1) [24]:

$$W(T) = \frac{m_0 - m(T)}{m_0} \times 100\% \quad (1)$$

TG was reported as normalized mass remaining and DTG as a positive time-based mass-loss rate (% min^{-1}); derivative scaling was verified against β(dm/dT). A fixed 21-point Savitzky–Golay filter was applied before peak detection [25] (Supplementary Eqs. (S1)–(S6)) . For the 20 °C min^{-1} comparison, stage losses were obtained by boundary subtraction over the intervals from the first valid temperature to 150 °C, 150–400 °C, and 400–700 °C. These intervals served as study-defined reporting regions. The rate-specific endpoint is denoted $R_{700,\beta}$, and the Fig. 3/Fig. 9 values at 20 °C min^{-1} are denoted $R_{700,20}$. T_5%, T_{10}%, and T_{50}% were obtained by first-bracket linear interpolation without extrapolation [24]. Fractional conversion for kinetic and distributed-reactivity analyses was calculated over 150–700 °C using Eq. (2) [17]:

$$\alpha(T) = \frac{m_{150} - m(T)}{m_{150} - m_{700}} \tag{2}$$

Equation (2) defines the operational conversion coordinate between the masses recorded at 150 and 700 °C. Accordingly, Tα and $E_a(\alpha)$ are referenced to the rate-specific 700 °C endpoint, particularly for whole fruit, for which $R_{700,\beta}$ showed the largest cross-rate variation.

2.3.1. Analytical-support-screened isoconversional analysis

Apparent activation energies were estimated at α = 0.10–0.90 using the Friedman, KAS, FWO, and Starink linear forms [26-32]. The analysis was designed to resolve conversion-dependent variation in effective apparent energy demand while identifying conversion levels supported consistently by the four-rate dataset. All methods used the same four-rate Tα matrix, and agreement among the related integral forms was included as an internal consistency criterion:

$$\ln\left[\beta_i \left(\frac{d\alpha}{dT}\right)_{\alpha,i}\right] = \ln[A_\alpha f(\alpha)] - \frac{E_\alpha}{RT_{\alpha,i}} \tag{2a}$$

$$\ln\left(\frac{T_{\alpha,i}^2}{\beta_i}\right) = \frac{E_\alpha}{RT_{\alpha,i}} + C_{\alpha,\mathrm{KAS}} \tag{2b}$$

$$\ln\beta_i = C_{\alpha,\mathrm{FWO}} - \frac{1.0518E_\alpha}{RT_{\alpha,i}} \tag{2c}$$

$$\ln\left(\frac{\beta_i}{T_{\alpha,i}^{1.92}}\right) = C_{\alpha,\mathrm{Starink}} - \frac{1.0008E_\alpha}{RT_{\alpha,i}} \tag{2d}$$

Activation energies were obtained from the fixed-conversion regression slope sα as −Rsα, Rsα, −Rsα/1.0518, and −Rsα/1.0008 for Friedman, KAS, FWO, and Starink, respectively. Equation (2b) uses the negative of the conventional KAS ordinate $\ln(\beta_i/T_{\alpha,i}^2)$, giving a slope of +Eα/R. Temperatures were expressed in kelvin, and β and rate terms used a consistent time basis. Conversion levels were screened jointly using temperature ordering, regression quality, regression-derived SE(E_a) and pointwise 95% intervals, agreement among integral methods,

Friedman deviation, profile continuity, and TG–DTG correspondence. This screening links regression performance to the measured thermal response and provides a common basis for comparing the three preparations. The study-defined rules are reported in Supplementary Methods, Eqs. (S19)–(S28), and Supplementary Tables S15–S22.

2.3.2. Endpoint-sensitivity assessment

Endpoint sensitivity was assessed because the terminal mass used to define fractional conversion can influence fixed-conversion temperatures and apparent kinetic parameters when the high-temperature residual-solid tail is progressively incorporated [50]. With 150 °C retained as the lower boundary, conversion was recalculated for terminal temperatures T_f = 600, 650, and 700 °C using Eq. (2e), where β denotes the programmed heating rate. The 150–700 °C basis remained the primary analysis, whereas 600 and 650 °C were treated as sensitivity conditions.

$$\alpha_{\beta}^{(T_{\mathrm{f}})}(T) = \frac{m_{\beta}(T_{\mathrm{i}}) - m_{\beta}(T)}{m_{\beta}(T_{\mathrm{i}}) - m_{\beta}(T_{\mathrm{f}})}. \tag{2e}$$

For each preparation, heating rate, and endpoint, endpoint-conditioned α(T), Tα, and the Friedman rate input were recalculated directly from the original point-wise TG–DTG records. The endpoint-conditioned rate was obtained from Eq. (2f), and Tα was determined by the established first-bracket linear interpolation without extrapolation.

$$\left(\frac{d\alpha}{dt}\right)_{\beta}^{(T_{\mathrm{f}})} = -\frac{1}{m_{\beta}(T_{\mathrm{i}}) - m_{\beta}(T_{\mathrm{f}})}\frac{dm_{\beta}}{dt} = \beta\left(\frac{d\alpha}{dT}\right)_{\beta}^{(T_{\mathrm{f}})}. \tag{2f}$$

The Friedman, KAS, FWO, and Starink regressions and the established analytical-support criteria were then reapplied without modification. Endpoint robustness was evaluated from changes in E_a magnitude, trajectory direction, retained reliability classification, and the preparation ordering over the common α = 0.40–0.60 interval. Full endpoint-specific inputs, estimates, and study-defined sensitivity diagnostics are reported in Supplementary Eqs. (S29)–(S35), Supplementary Figure S16, and Supplementary Tables S29–S31

2.4. DTG peak-domain analysis and conditional decomposition

Peak position, raw height, prominence, and recurrence were evaluated over 100–420 °C. Eligible peaks required separation ≥25 °C and prominence ≥ max[0.04ΔDTG, cβ], where ΔDTG is the within-curve DTG range and cβ = 0.02% °C^{-1}; when β is expressed in °C min^{-1}, the second term has units of % min^{-1}. A domain was classified as recurring when detected across the programmed heating rates without order reversal; remaining features were recorded as rate-specific shoulders. These study-defined thresholds standardized peak selection. For feedstocks exhibiting two recurring domains, relative peak height and inter-domain separation

were calculated using Eqs. (3) and (4), with the lower- and higher-temperature domains ordered by peak temperature [33,34]:

$$R_H = \frac{H_{p,2}}{H_{p,1}} \tag{3}$$

$$\Delta T_p = T_{p,2} - T_{p,1} \tag{4}$$

Peak-height ratios, peak separations, and their cross-rate summaries were used descriptively [35,36]; (Supplementary Eq. (S7)). Kissinger analysis (Supplementary Eq. (S8)) was restricted to tracked domains with $R^2 \geq 0.95$ [37], and the resulting $E_{K,p}$ values served as secondary peak-shift diagnostics [38]. Baseline-corrected DTG curves for the two-domain feedstocks were fitted conditionally over 100–450 °C with one to three symmetric Gaussian components. Because the baseline was removed before fitting, Eqs. (5)–(6) contain only the Gaussian sum. The analysis evaluated empirical shape adequacy without constituent assignment [39]:

$$\hat{y}(T) = \sum_{j=1}^{K_G} G_j\,(T) \tag{5}$$

$$G_j(T) = \frac{A_{G,j}}{\sigma_{T,j}\sqrt{2\pi}} \exp\left[-\frac{\left(T - \mu_{T,j}\right)^2}{2\sigma_{T,j}^2}\right] \tag{6}$$

Gaussian areas were constrained to non-negative values; center temperatures, widths, and adjacent-center separation were restricted to 100–450 °C, 5–120 °C, and ≥20 °C, respectively. Eight multistart optimizations were performed per candidate, and the converged minimum-RSS solution was retained. FWHM, AICc, and BIC were calculated using Supplementary Eqs. (S9)–(S13) with a common observation set and error definition [40]. Candidate complexity was selected jointly from information-criterion ranking, residual behavior, convergence, boundary checks, and cross-rate stability. AICc and BIC were used for relative ranking within the tested candidate set.

2.5. Distributed-reactivity modeling and model-adequacy assessment

Multirate TG data for seed, skin, and whole fruit were modeled independently over 150–700 °C, with active-interval mass normalized at 150 °C. Whole-fruit behavior was modeled directly rather than reconstructed from isolated fractions. Seed and skin used all four heating rates and permitted leave-one-rate-out cross-condition prediction. For whole fruit, the 20 °C min^{-1} curve exceeded the study-defined $R_{700,\beta}$ consistency criterion; DAEM calibration therefore used 5, 10, and 15 °C min^{-1}, while all four rates remained in the measured TG–DTG and isoconversional analyses. The 20 °C min^{-1} curve was retained in those measured and fixed-conversion analyses because it passed conversion-bound and TG–DTG derivative-consistency checks; endpoint sensitivity was evaluated separately, while its larger R_{700} spread remains a

replicate/sample-homogeneity verification flag rather than evidence attributable solely to heating rate (Supplementary Tables S5, S8, S9, and S15). Model appraisal combined global fit, signed and serial residuals, multistart convergence, boundary contact, parameter stability, model-derived DTG shape, and, for seed and skin, withheld-rate performance.

A parallel first-order Gaussian DAEM was used. The activation-energy density and active-interval normalization are given in Supplementary Eqs. (S14)–(S15), and conversion at fixed activation energy was calculated using Eq. (7) [23]:

$$\frac{d\alpha_{rj}(T,E;\beta)}{dT} = \frac{A_{rj}}{\beta}\exp\left(-\frac{E}{RT}\right)\left[1-\alpha_{rj}(T,E;\beta)\right] \qquad \alpha_{rj}(T_0,E;\beta)=0 \tag{7}$$

Temperature was expressed in kelvin, T_0 = 423.15 K, and A and β used the same time basis. Distribution-averaged domain conversion was calculated using Eq. (8) with the positive-energy-normalized density defined in Supplementary Eq. (S15) [23]:

$$\overline{\alpha}_{rj}(T,\beta) = \int_0^{\infty} D_{rj}(E)\,\alpha_{rj}(T,E;\beta)\,dE \tag{8}$$

The distribution-averaged conversion was treated as a model-derived reactivity coordinate. Predicted normalized mass was obtained using Eq. (9) [23]:

$$\widehat{m}_{r,\beta}(T) = 1-\sum_{j=1}^{K} c_{rj}\,\overline{\alpha}_{rj}(T,\beta) \qquad c_{rj}\geq 0, \quad \sum_{j=1}^{K} c_{rj}\leq 1 \tag{9}$$

The non-negative capacity coefficients describe post-150 °C mass-loss capacities. One-, two-, and three-domain candidates were fitted simultaneously across the retained heating rates using the equal-rate-weighted least-squares objective in Eq. (10) [23,41]:

$$J_{r,K}(\theta_{r,K}) = \frac{1}{|\mathcal{B}_{\mathrm{fit}}|}\sum_{\beta\in\mathcal{B}_{\mathrm{fit}}}\frac{1}{N_{r,\beta}}\sum_{i=1}^{N_{r,\beta}}\left[m_{r,\beta}^{\mathrm{obs}}(T_i)-\widehat{m}_{r,\beta}(T_i;\theta_{r,K})\right]^2 \qquad \hat{\theta}_{r,K} = \underset{\theta_{r,K}\in\Theta_{r,K}}{\arg\min}\, J_{r,K}(\theta_{r,K}) \tag{10}$$

Multistart optimization and ordered centers were used to limit local-minimum and label-switching effects. The model notation, active-interval normalization, parameter constraints, activation-energy density, predicted-DTG relation, and fit diagnostics are reported in Supplementary Section S3. Model retention required joint support from calibration error,

residual structure, convergence, parameter stability, boundary behavior, model-derived DTG shape, and withheld-rate prediction.

For seed and skin, each heating rate was withheld sequentially; the model was fitted to the other three curves and the excluded curve was predicted without retuning. Prediction RMSE was calculated using Eq. (11) [23]:

$$\mathrm{RMSE}_{r,K}^{\mathrm{pred},(-\beta_h)} = 100\left[\frac{1}{N_{r,\beta_h}}\sum_{i=1}^{N_{r,\beta_h}}\left\{m_{r,\beta_h}^{\mathrm{obs}}(T_i) - \hat{m}_{r,\beta_h}\left[T_i;\hat{\theta}_{r,K}^{(-\beta_h)}\right]\right\}^2\right]^{1/2}$$
$$\hat{\theta}_{r,K}^{(-\beta_h)} = \underset{\theta_{r,K}\in\Theta_{r,K}}{\arg\min}\, J_{r,K}^{(-\beta_h)}\left(\theta_{r,K}\right) \tag{11}$$
$$\mathcal{B}_{(-\beta_h)} = \{\beta \in \mathcal{B}: \beta \neq \beta_h\}$$

All four seed and skin folds were reported individually and summarized by mean, median, and worst RMSE together with parameter stability. The folds were interpreted as cross-condition prediction tests. Prediction-supported performance required consistent withheld-rate behavior, parameter stability, residual structure, and derivative-shape fidelity. Whole-fruit DAEM results were reported as a three-rate calibration model.

3. Results and discussion

3.1 Thermal decomposition behavior and analytical-support-screened kinetic analysis of rosehip feedstocks

3.1.1 TG–DTG behavior (β = 5–20 °C min⁻¹)

Raising β from 5 to 20 °C min^{-1} displaced the TG–DTG profiles toward higher temperatures (Fig. 2). The corresponding increases in $T_{5\%}$, $T_{10\%}$, and $T_{50\%}$ were 47.7, 37.7, and 26.0 °C for rosehip seed; 33.4, 32.4, and 20.9 °C for rosehip skin; and 20.9, 29.4, and 17.0 °C for whole-fruit rosehip, respectively (Supplementary Table S4). This rightward displacement is consistent with the reduced time available for conversion at a given temperature and increased sample–furnace thermal lag at higher heating rates, causing equivalent mass-loss levels and DTG features to occur at higher measured temperatures [8,9,17]

Isola et al. [42] and Castro et al. [43] report $T_{5\%}$, $T_{10\%}$, and $T_{50\%}$ as temperatures corresponding to fixed mass-loss levels, whereas Wang et al. [44] uses $T_{5\%}$ as an initial decomposition threshold. Accordingly, these characteristic temperatures are treated here as operational indices for comparing the onset and progression of thermal decomposition rather than as unique reaction temperatures or constituent-specific boundaries Because dα/dt = β(dα/dT), the increase in time-based DTG amplitude partly reflects derivative scaling; peak height was therefore interpreted together with peak position and recurrence [45]. Seed exhibited the most delayed conversion. Across 5–20 °C min^{-1}, $T_{5\%}$, $T_{10\%}$, and $T_{50\%}$ increased from 180.3 to 228.0 °C, 231.2

to 268.9 °C, and 342.3 to 368.3 °C, respectively; the principal DTG maximum shifted from 332 to 360 °C, and $DTG_{t,max}$ increased from 3.598 to 14.060% min^{-1} (Supplementary Tables S1 and S4). Together, the high T_5% values and the recurring 332–360 °C domain identify seed as the most thermally delayed and comparatively concentrated preparation. Except for a 278 °C feature at 10 °C min^{-1}, seed retained a recurring higher-temperature envelope (Supplementary Table S3). This multi-event behavior is consistent with the four thermal effects reported for raw *Rosa rubiginosa* seeds by Martín-Ramos et al.[11] and with the moisture-loss process plus three deconvoluted pyrolysis reactions identified for exhausted rosehip seed waste by Torres-Sciancalepore et al.[12]. Because biomass constituents decompose over overlapping temperature ranges, the dominant maximum is interpreted as a thermal domain rather than assigned to a single constituent [6,46].

Skin decomposed earlier but retained a higher-temperature contribution. $T_{5\%}$, $T_{10\%}$, and $T_{50\%}$ increased from 141.8 to 175.1 °C, 165.5 to 197.9 °C, and 351.4 to 372.3 °C, respectively (Supplementary Table S4). At 20 °C min^{-1}, the two maxima occurred near 223 and 336 °C, with tracked lower- and higher-temperature positions of 222 and 335 °C, respectively (Supplementary Tables S3 and S10). The two recurring domains show that earlier conversion in skin coexisted with a substantial higher-temperature response. Changes in the relative prominence of the two domains produced the non-monotonic principal-maximum sequence; the maxima at 5 and 10 °C min^{-1} were therefore treated as co-dominant (Supplementary Tables S4, S10, and S11). The skin maxima are therefore interpreted as overlapping thermal domains rather than as separate constituent reactions.

Whole-fruit rosehip coupled the earliest low-conversion response with a recurring higher-temperature maximum. Across 5–20 °C min^{-1}, $T_{5\%}$ and $T_{10\%}$ increased from 116.0 to 136.9 °C and 164.5 to 193.9 °C, respectively. $T_{50\%}$ rose from 338.6 °C at 5 °C min^{-1} to 357.9 °C at 15 °C min^{-1} and then decreased slightly to 355.6 °C at 20 °C min^{-1} (Supplementary Tables S1 and S4). The coexistence of the earliest T_5% values with a recurring higher-temperature maximum shows that early mass loss did not define the dominant conversion domain. The principal higher-temperature maximum shifted from 334 to 352 °C between 5 °C min^{-1} and 15 °C min^{-1} and occurred at 351 °C at 20 °C min^{-1}, where a lower-temperature maximum was detected at 225 °C (Supplementary Tables S1 and S3). The coexistence of lower- and higher-temperature features is consistent with distinct thermal responses previously reported for rosehip tissues and pomace. Whole-fruit behavior was therefore interpreted directly as an integrated preparation rather than reconstructed from isolated fractions[11,16]. Because anatomical mass fractions and a separate pulp/flesh curve were unavailable, the whole-fruit response was evaluated directly rather than through additive reconstruction or interaction testing.

Thermal ordering was descriptor-dependent. At 20 °C min^{-1}, $T_{5\%}$ ranked seed (228.0 °C) > skin (175.1 °C) > whole fruit (136.9 °C), whereas $T_{50\%}$ ranked skin (372.3 °C) > seed (368.3 °C) > whole fruit (355.6 °C) (Supplementary Table S4). Seed therefore showed the most delayed low-conversion response, skin retained competing lower- and higher-temperature domains, and whole-fruit rosehip combined early mass loss with a dominant higher-temperature domain (Supplementary Table S3). Because heterogeneous biomass conversion comprises overlapping processes, fixed-loss temperatures, DTG maxima, peak multiplicity, and residual mass provide complementary descriptors. The reversal between the T_5% and T_{50}% rankings therefore shows that no single stability descriptor captures the complete thermal response [47].

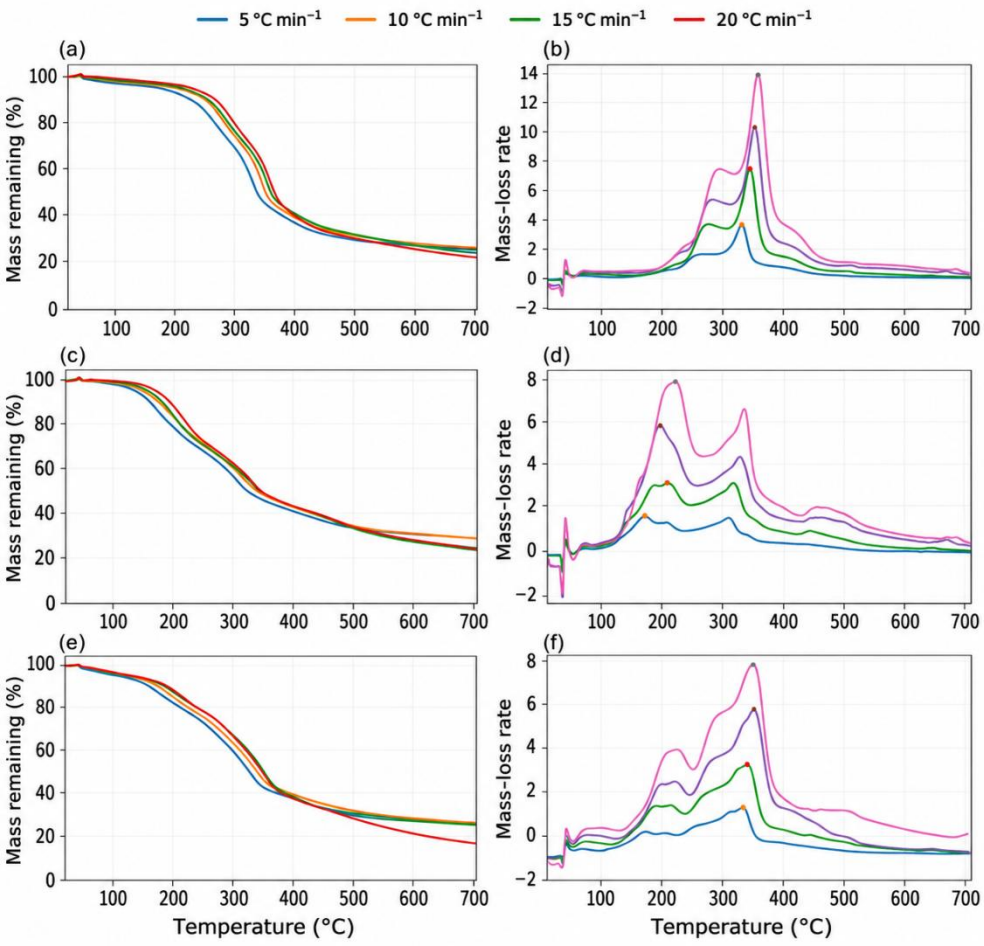


Fig. 2. TG (a,c,e) and time-based DTG (% min^{-1}; b,d,f) profiles of rosehip seed (a,b), skin (c,d) and whole fruit (e,f) at 5–20 °C min^{-1}.

At 20 °C min^{-1}, the fixed temperature-interval comparison differentiated the feedstocks (Fig. 3; Supplementary Table S2). Stage I, Stage II, and Stage III refer exclusively to the predefined intervals ending at 150, 400, and 700 °C, respectively, and are not constituent-specific or peak-onset-defined reaction stages. Stage I captures low-temperature mass loss rather than a constituent-specific process. Within this interval, whole fruit showed a distinct contribution, whereas seed and skin remained similar [11,17] (Supplementary Table S2). Stage II dominated mass loss in seed (56.85%), whole fruit (53.27%), and skin (50.95%),

although comparable interval totals corresponded to distinct DTG architectures. Stage III losses were 20.10%, 18.21%, and 17.30% for whole fruit, seed, and skin, respectively, whereas R_{700} ranked skin (29.97%) > seed (22.91%) > whole fruit (20.93%) (Supplementary Table S2). The R_{700} ordering complements the characteristic-temperature and DTG-domain results by describing the extent of mass retained after the full TGA program.

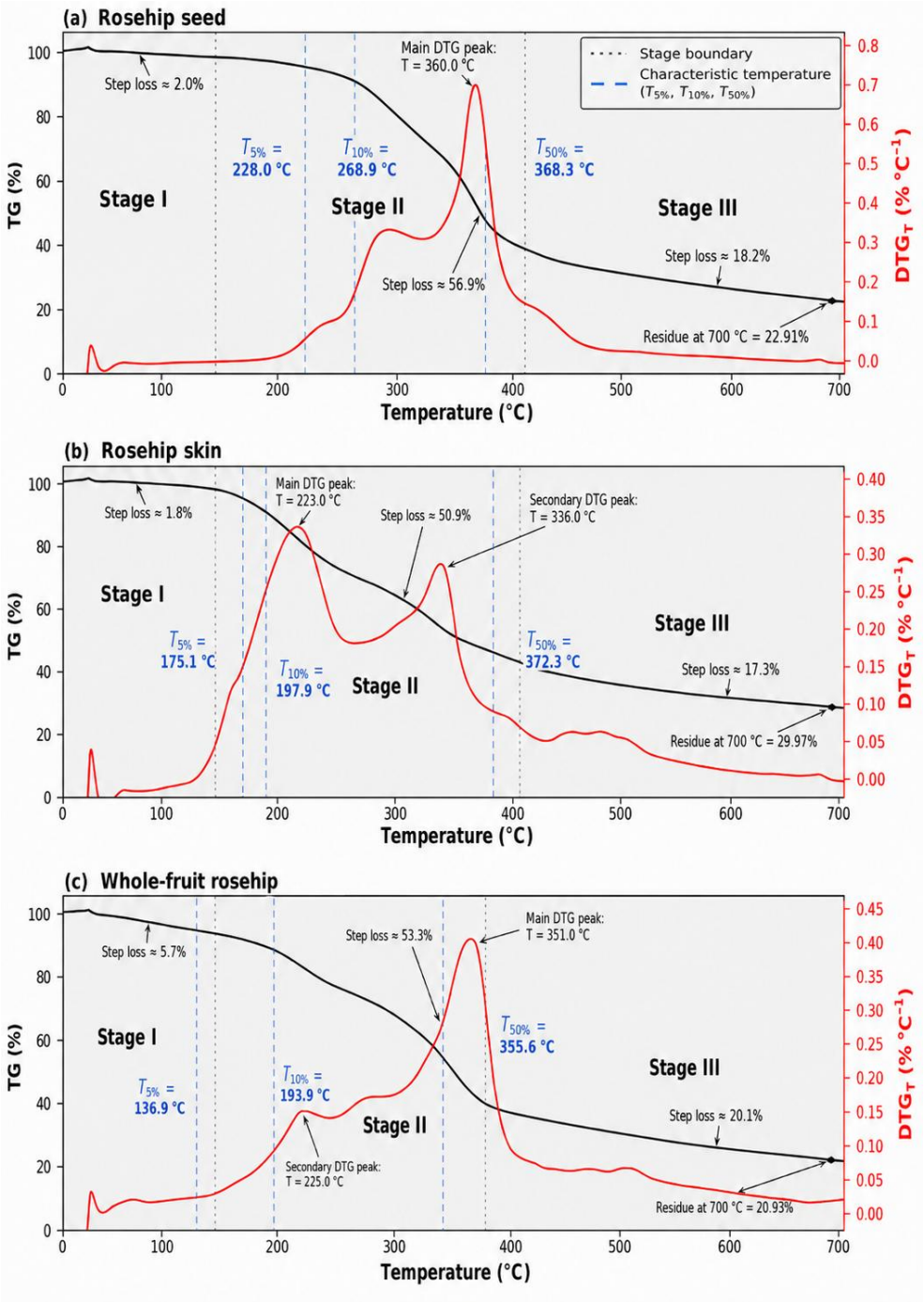


Fig. 3. Stage-resolved TG and temperature-based DTG (% °C^{-1}) profiles of rosehip seed (a), skin (b) and whole fruit (c) at 20 °C min^{-1} using fixed comparative intervals of <150, 150–400 and 400–700 °C.

Across heating rates, R_{700} varied by 3.88 percentage points for seed, 4.11 for skin, and 8.51 for whole fruit; only the whole-fruit range exceeded the study-defined 5.0-percentage-point consistency threshold (Supplementary Table S5). The larger whole-fruit variation is therefore treated as a quality-control signal requiring replicate and sample-homogeneity verification before being attributed solely to heating rate. It also shows that the endpoint-normalized conversion coordinate changed more strongly across the whole-fruit runs than across the seed and skin runs. Because R_{700} is the endpoint used to normalize conversion between 150 and 700 °C, whole-fruit $T\alpha$ and $E_a(\alpha)$ values are reported on an endpoint-conditioned conversion basis. Within the investigated TGA conditions, seed exhibited delayed conversion and a higher-temperature envelope, skin showed more distributed decomposition and the highest R_{700}, and whole fruit combined the earliest $T_5\%$ with the lowest R_{700} at 20 °C min^{-1}. $T\alpha = 0.50$ was 16.1–18.1 °C lower than $T_{50}\%$ for seed, 65.0–74.6 °C lower for skin, and 20.6–34.7 °C lower for whole fruit (Supplementary Tables S6 and S7). The offset arises because $T\alpha$ is referenced to the 150–700 °C active interval, whereas $T_{50}\%$ is referenced to the initial sample mass; the two temperatures therefore describe different conversion coordinates.

3.1.2 Recurring cross-rate DTG-domain analysis

Across the four programmed heating rates, the adopted peak-selection rules identified one recurring domain for seed and two for skin and whole fruit (Supplementary Tables S10–S12). This one-versus-two-domain contrast shows that the preparations differed not only in conversion temperature but also in how mass-loss activity was distributed across the thermal program. A recurring domain was defined operationally as a peak feature detected across all four heating rates; recurrence therefore denotes cross-rate persistence rather than constituent identity. For skin, the synthesis envelopes of 173–223 and 310–336 °C include both raw and algorithm-tracked maxima; the corresponding filtered ranges in Fig. 4 were 173–222 and 310–335 °C. Peak-height ratio identified the dominant domain, while inter-domain separation quantified the thermal spacing between the two responses.

Seed preserved a recurring higher-temperature domain that shifted from 332 to 360 °C between 5 and 20 °C min^{-1} (mean 348.0 ± 12.11 °C; range 28 °C). Peak height and prominence increased from 3.598 to 14.060% min^{-1} and from 2.944 to 10.871% min^{-1}, respectively (Supplementary Tables S10 and S12). The preserved higher-temperature position, together with increasing time-based peak intensity, shows that heating rate changed the apparent conversion rate more strongly than the location of the dominant seed domain. The isolated 278 °C feature at 10 °C min^{-1} did not recur and was therefore retained as a rate-specific feature. Skin retained algorithm-tracked lower- and higher-temperature positions at 173–222 and 310–335 °C, with means of 201.0 ± 21.09 and 322.75 ± 11.00 °C, respectively. Raw maxima at 20

°C min⁻¹ occurred at 223 and 336 °C (Fig. 3), accounting for the one-degree extension of the synthesis envelopes. The 13 °C downward shift of the lower-temperature maximum between 10 and 15 °C min⁻¹ is consistent with overlap-sensitive movement within a broad thermal envelope rather than emergence of a new domain [33]. A peak-height ratio below unity at every rate (0.750–0.998; mean 0.884) establishes persistent lower-temperature dominance or co-dominance, while the 107–137 °C separation confirms two distinct thermal envelopes (Supplementary Tables S10–S12). Compared with skin, whole fruit showed higher-temperature domain dominance. Its lower- and higher-temperature domains occurred at 174–225 and 333–352 °C, with means of 208.75 ± 23.63 and 344.25 ± 9.00 °C, respectively. In contrast to skin, the peak-height ratio of 1.807–2.013 (mean 1.899) establishes persistent higher-temperature dominance in whole fruit. The decrease in inter-domain separation from 159 °C at 5 °C min⁻¹ to 126–130 °C at 10–20 °C min⁻¹ shows convergence of the domain positions while preserving the two-domain architecture (Supplementary Tables S10–S12). Whole fruit therefore retained a two-domain architecture weighted toward higher-temperature conversion. Domain positions varied less than time-based peak height and prominence, indicating that heating rate altered response intensity more strongly than domain identity (Supplementary Table S12). Despite similar Stage II mass losses, skin and whole fruit showed opposite domain dominance, demonstrating that interval totals alone do not describe how conversion was distributed across temperature (Fig. 4; Supplementary Table S2).

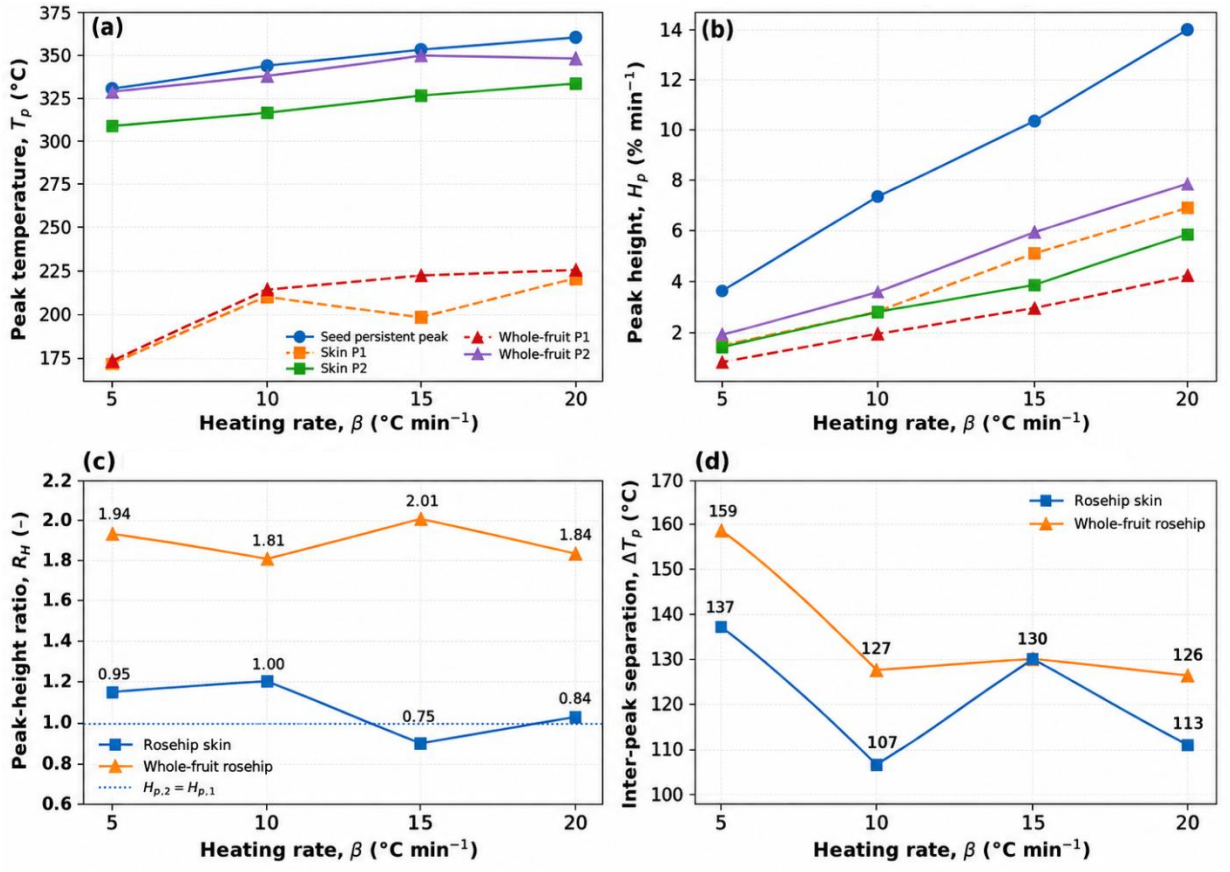


Fig. 4. Heating-rate dependence of algorithm-tracked recurring DTG-domain positions (a), domain-maximum heights (b), peak-height ratios (c) and inter-domain separation (d) for rosehip seed, skin and whole fruit

Only the seed domain and the higher-temperature skin domain met the predefined tracking criterion, yielding Kissinger apparent activation energies of 147.60 kJ mol^{-1} (R^2 = 0.9998) and 148.56 kJ mol^{-1} (R^2 = 0.9619), respectively. Their near-equality reflects similar heating-rate displacement of the tracked maxima rather than kinetic equivalence between the two preparations [37] (Fig. 5; Supplementary Table S13). Their numerical similarity reflects comparable peak-shift regression slopes and does not imply a shared reaction pathway. Given the four-point heating-rate span (βmax/βmin = 4), the retained Kissinger values are used as peak-shift descriptors rather than as tests of single-step behavior or conversion dependence. They therefore complement the conversion-resolved isoconversional analysis, while the remaining domain regressions are reported in Supplementary Figure S2 and Supplementary Table S13 [38].

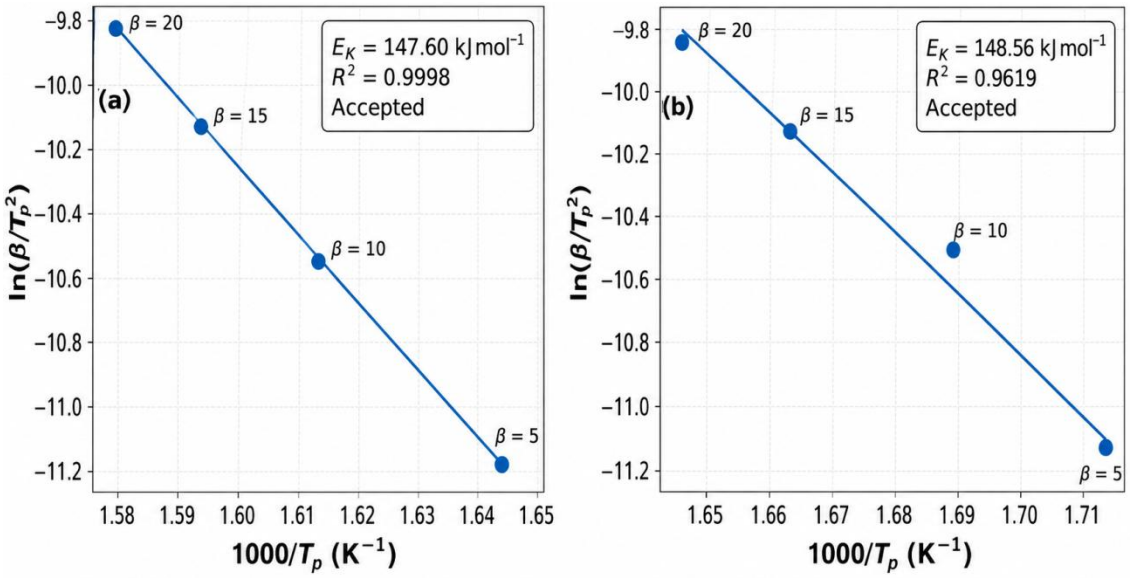


Fig. 5. Four-point Kissinger regressions for the tracked recurring rosehip-seed domain (a) and tracked higher-temperature rosehip-skin domain (b)

AICc and BIC favored three-component candidates for skin and whole fruit, but the fitted residuals remained strongly serial (|r_1| = 0.9865–0.9912; runs-test $p < 0.001$), and several candidates lacked multistart or cross-rate stability (Supplementary Table S14; Supplementary Figure S4). Thus, additional Gaussian components improved relative fit ranking without reproducing the measured derivative structure adequately [40]. Recurring-domain analysis was therefore retained as the primary description, whereas the Gaussian terms were interpreted only as empirical shape components rather than mechanisms, tissues, or constituents [47].

3.1.3 Analytical-support-screened isoconversional analysis

Conversion-resolved apparent activation-energy profiles, $E_a(\alpha)$, showed that the three preparations differed not only in mean apparent energy demand but also in how that demand evolved with conversion. Because $E_a(\alpha)$ is an effective isoconversional quantity, its variation is interpreted as a change in the overall reacting population rather than as a sequence of elementary activation barriers. Interpretation was therefore restricted to conversion levels supported jointly by temperature ordering, regression behavior, inter-method agreement, profile continuity, and TG–DTG correspondence. [19,48]. Complete inputs, estimates, and classifications are reported in Supplementary Tables S15–S22. Seed exhibited the broadest principal analytically supported interval (α = 0.10–0.70; Fig. 6a). Integral $E_a(\alpha)$ increased from 99.25 kJ mol^{-1} at α = 0.10 to 142.04 kJ mol^{-1} at α = 0.40 and remained within 142.04–147.16 kJ mol^{-1} through α = 0.70. The integral-method mean was 133.41 kJ mol^{-1} and the Friedman mean was 139.24 kJ mol^{-1}; the KAS, FWO, and Starink estimates remained closely grouped. The rise followed by a narrow high-conversion plateau shows that seed progressed from a lower apparent energy requirement at early conversion to a comparatively uniform effective-energy regime during its central conversion interval. At α = 0.70, the Friedman regression weakened (R^2 = 0.7655), whereas the integral methods retained $R^2 \geq 0.9474$. Accordingly, α = 0.40–0.70 represents a comparatively stable apparent-energy regime, while the weakening Friedman regression at α = 0.70 prevents interpreting this interval as a single-step reaction (Supplementary Tables S19–S22) [49].

Seed estimates at α = 0.80–0.90 were classified as low confidence: the minimum integral R^2 values were 0.8794 and 0.8746, and the inter-method CV reached 5.97% at α = 0.90. Both points lay in the high-temperature tail. Integral E_a declined from 147.16 kJ mol^{-1} at α = 0.70 to 138.02 and 77.82 kJ mol^{-1} at α = 0.80 and 0.90, respectively. The late decline coincided with the high-temperature tail, weaker regressions, and greater method sensitivity. These values therefore describe reduced analytical support at the conversion endpoint rather than evidence of a lower intrinsic reaction barrier [50,51] (Supplementary Tables S16 and S19–S21).

Skin displayed the strongest conversion dependence (Fig. 6b). The α = 0.10 point was analytically supported but isolated, whereas α = 0.20–0.30 was classified as low confidence because the minimum integral R^2 values were 0.892–0.894 and Friedman exceeded the integral means by 20.9–22.8%. Across the principal analytically supported interval α = 0.40–0.60, integral E_a decreased from 277.22 to 191.19 and 152.21 kJ mol^{-1}, yielding a descriptive mean of 206.87 kJ mol^{-1}; Friedman reproduced the decline with a mean of 186.16 kJ mol^{-1}. This pronounced decline shows that the high apparent energy demand at the beginning of the retained interval was not sustained as conversion progressed, consistent with a changing

contribution of overlapping reacting populations [48]. A single global activation energy would therefore conceal the strongest conversion dependence observed among the three preparations, although the $E_a(\alpha)$ trajectory alone cannot identify constituent-specific transitions (Tables S17 and S19–S22) [38,48]. Skin estimates at α = 0.70–0.90 remained low confidence (minimum integral R^2 = 0.782–0.833). At α = 0.70, T_α decreased from 376.0 °C at 15 °C min^{-1} to 368.2 °C at 20 °C min^{-1}, exceeding the study-defined 5 °C fixed-conversion backshift tolerance. Because the α = 0.70 temperature backshift disrupted the expected cross-rate ordering, the late-conversion values were retained as low-confidence diagnostics rather than used to extend the decreasing kinetic trajectory (Supplementary Tables S16–S17 and S19–S21).

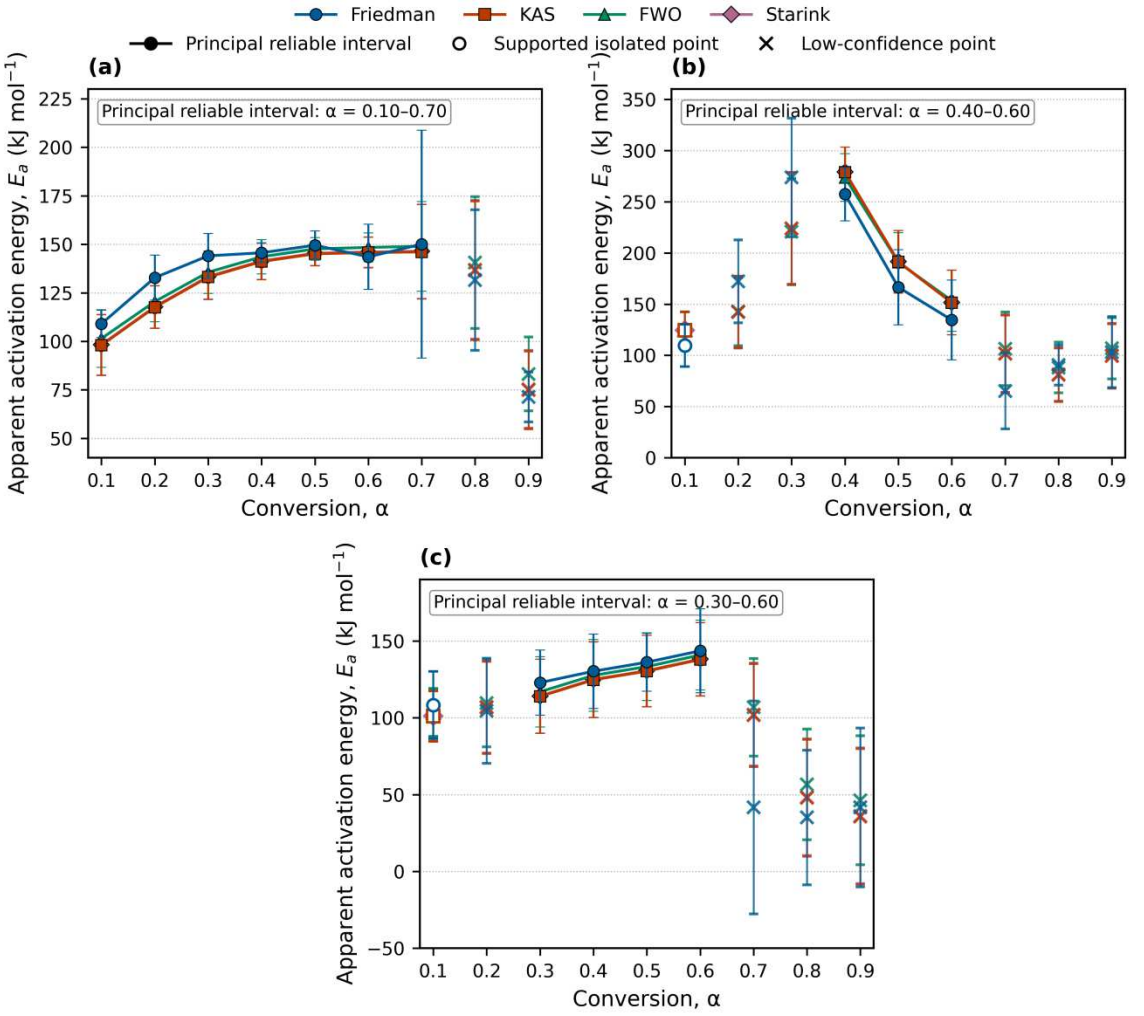


Fig. 6. Conversion-dependent apparent activation energies for rosehip seed (a), skin (b) and whole fruit (c) determined by the Friedman, KAS, FWO and Starink methods.

Whole-fruit rosehip showed an endpoint-conditional increasing trajectory (Fig. 6c). The α = 0.10 point was analytically supported but isolated, α = 0.20 was classified as low confidence, and the principal analytically supported interval was α = 0.30–0.60. Integral E_a increased from 115.02 to 139.04 kJ mol^{-1} and averaged 127.83 kJ mol^{-1}; Friedman averaged 133.25 kJ mol^{-1}. The integral regressions yielded minimum R^2 values of 0.918–0.944, although the KAS, FWO, and Starink estimates remained closely grouped. Within the retained interval, the increasing

trajectory shows that progressively later conversion required greater effective apparent energy on the adopted endpoint-conditioned basis. Because R_{700} varied most strongly for whole fruit, this increasing trajectory describes the operational 150–700 °C conversion coordinate and should not be generalized beyond that normalization basis (Supplementary Tables S17 and S19–S22). Above α = 0.60, whole-fruit estimates were classified as low confidence. At α = 0.70, Friedman decreased to 41.66 kJ mol^{-1}, whereas the integral-method mean remained 103.58 kJ mol^{-1}, a 59.8% deviation. At α = 0.80 and 0.90, the minimum integral R^2 values declined to 0.443 and 0.247, respectively, while the inter-method CV increased to 9.61 and 15.10%. The combination of severe method divergence and weak integral regressions shows that these late-conversion estimates no longer represented a stable cross-rate kinetic relationship (Supplementary Tables S17 and S19–S21).

Across the retained conversion levels, KAS and Starink estimates were nearly coincident, whereas FWO was slightly higher. This pattern is consistent with the shared temperature-integral basis of these linear integral methods and the different approximations used to evaluate it [27]. Because KAS, FWO, and Starink used the same Tα matrix, their agreement demonstrates internal consistency among related integral approximations rather than independent validation. Friedman broadly preserved the feedstock-specific trajectory shapes but showed larger pointwise deviations, reflecting the greater sensitivity of differential analysis to local rate data [19,51]. The root-mean-square standard errors of E_a were 12.83–13.52 kJ mol^{-1} for the integral methods versus 24.28 kJ mol^{-1} for Friedman in seed, 27.52–28.95 versus 34.40 kJ mol^{-1} in skin, and 22.76–23.98 versus 23.14 kJ mol^{-1} in whole fruit. The generally larger Friedman errors reinforce its role as a supportive trajectory check rather than the sole basis for defining the retained kinetic intervals. These values summarize fixed-conversion regression precision across the four programmed heating rates (Supplementary Tables S17, S19, and S22).

3.1.4 Endpoint robustness of preparation-specific $E_a(\alpha)$ trajectories

Endpoint recalculation at Tf = 600, 650, and 700 °C altered the absolute apparent activation energies but preserved the preparation-specific principal trajectory directions (Table 1; Supplementary Figure S16; Supplementary Tables S29–S31). Seed remained increasing over α = 0.10–0.70, skin remained decreasing over α = 0.40–0.60, and whole fruit remained increasing over α = 0.30–0.60. Across the common interval α = 0.40–0.60, the integral-method mean ordering remained skin > seed > whole fruit at every endpoint. The differentiation among preparations was therefore independent of the selected terminal-mass definition.

Magnitude sensitivity was greatest for skin. As Tf increased from 600 to 700 °C, the descriptive principal-window means decreased from 141.83 to 133.41 kJ mol^{-1} for seed, from

261.30 to 206.87 kJ mol^{-1} for skin, and from 138.19 to 127.83 kJ mol^{-1} for whole fruit. This endpoint dependence is consistent with the terminal-temperature sensitivity reported for beech-wood pyrolysis, where changing the selected final temperature altered the conversion coordinate and the derived kinetic parameters; the divergence at high conversion was attributed to the progressively greater contribution of slow residual-char degradation at higher temperatures [50]. The largest pointwise endpoint ranges within the reference intervals were 19.23 kJ mol^{-1} for seed at α = 0.70, 67.34 kJ mol^{-1} for skin at α = 0.40, and 12.24 kJ mol^{-1} for whole fruit at α = 0.60. The skin result at Tf = 600 °C and α = 0.40 was classified as low-confidence (minimum integral-method R^2 = 0.8639), whereas all other reference-window points were classified as reliable. Accordingly, the 600 °C skin mean is conditional. The endpoint-robust findings are the trajectory directions and shared-window ordering; the absolute E_a values remain conversion-coordinate dependent.

Table 1. Reference principal conversion intervals and endpoint sensitivity of integral-method apparent activation-energy trajectories

Feedstock	**Reference principal interval (700 °C basis)**	**Mean integral E_a at T_f = 600/650/700 °C (kJ mol^{-1})**	**Trajectory direction at T_f = 600/650/700 °C**	**Maximum pointwise endpoint range within the reference interval**
Seed	α = 0.10–0.70	141.8 / 137.4 / 133.4	Increasing at all three endpoints	19.2 kJ mol^{-1} at α = 0.70
Skin	α = 0.40–0.60	261.3 / 235.1 / 206.9	Decreasing at all three endpoints	67.3 kJ mol^{-1} at α = 0.40
Whole fruit	α = 0.30–0.60	138.2 / 132.7 / 127.8	Increasing at all three endpoints	12.2 kJ mol^{-1} at α = 0.60

3.2 Distributed-reactivity modeling and model-adequacy assessment

Gaussian distributed activation energy models (DAEMs; *K* = 1–3) were fitted to TG data over 150–700 °C. The central modelling question was whether increasing Gaussian complexity merely reduced TG error or also produced a stable representation that transferred across heating conditions and preserved the measured derivative structure. Within this global TG formulation, the Gaussian distributions were interpreted as formal reactivity populations rather than biochemical or anatomical constituents [52,53]. Full statistics and diagnostics are reported in Supplementary Tables S23–S28 and Supplementary Figures S5–S15. Increasing K reduced RMSE and generally improved the nominal AICc/BIC rankings. Accordingly, numerical improvement with increasing K was treated as preliminary evidence rather than as proof of model adequacy. Because information criteria provide relative comparisons within the specified candidate set, model adequacy was evaluated jointly from residual structure, multistart stability, parameter-bound contact, derivative-shape fidelity, and cross-rate behavior

[40]. This broader appraisal was necessary because activation-energy/pre-exponential-factor compensation can produce similarly close fits from materially different parameter combinations [52,54].

For rosehip seed, $K = 2$ provided the most defensible reduced-order representation. Relative to $K = 1$, global RMSE decreased from 2.025 to 1.095 percentage points and mean withheld-rate RMSE from 2.133 to 1.315 percentage points. Although $K = 3$ further reduced these values to 0.952 and 1.219 percentage points, respectively, its near-optimal solutions showed practical non-identifiability: one activation-energy center and one distribution width contacted their imposed bounds, while the spreads in center position and pre-exponential factor reached 61.25 kJ mol^{-1} and 5.31 log_{10} units. The $K = 2$ calibration captured the overall multirate TG displacement but retained systematic deviations in the conversion and terminal regions (Fig. 7a). Leave-one-heating-rate-out predictions, generated by refitting the remaining three rates, gave a mean T_{50} prediction error of 3.27 K and showed reduced fidelity near the terminal portion of the curves (Fig. 7b). Thus, K = 2 produced a substantial improvement over K = 1, whereas the additional numerical gain from K = 3 was comparatively small and had to be weighed against parameter stability. Signed residuals remained structured and heating-rate dependent (Fig. 7c), and the model-derived DTG displaced or omitted several measured derivative features. The retained model therefore represented the dominant multirate mass-conversion trend rather than every measured derivative feature (Fig. 7d). Taken together, the fit improvement, greater parameter stability, and partial cross-rate transfer supported K = 2 as the parsimonious descriptive model for seed (Supplementary Tables S24–S25; Supplementary Figures S5–S8).

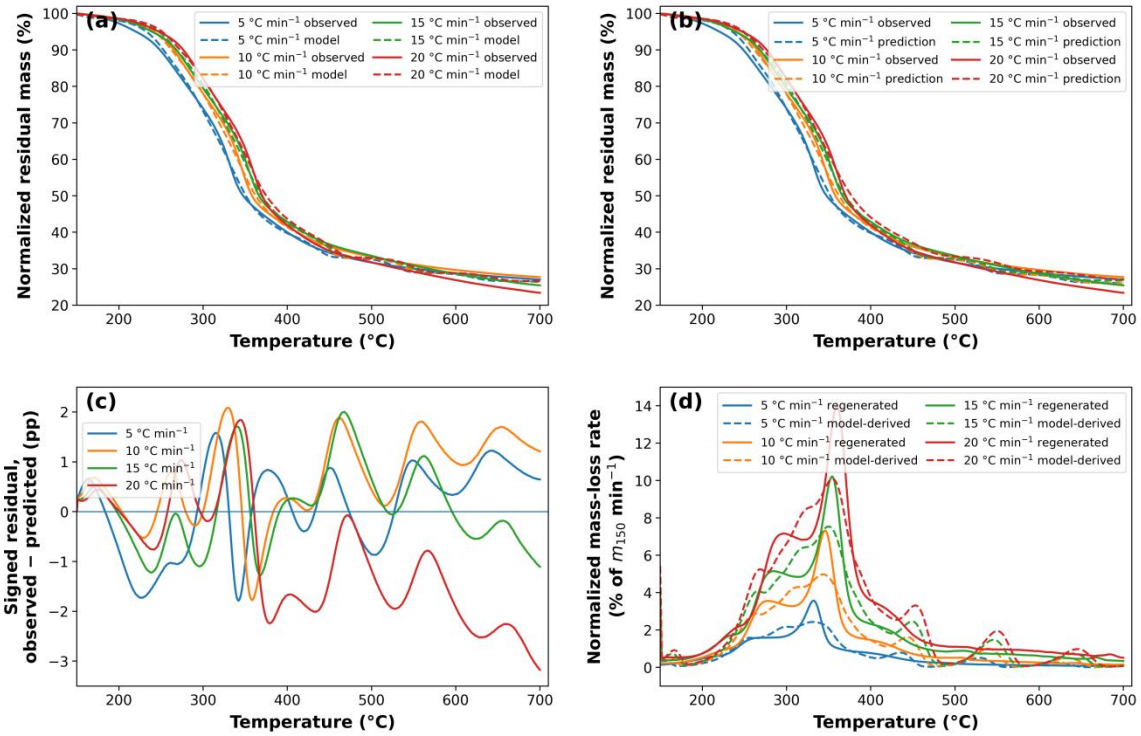


Fig. 7. Two-domain DAEM assessment of rosehip seed: multirate TG calibration (a), leave-one-rate-out cross-condition prediction assembled from four separately refitted models (b), signed residuals (c), and measured-TG-derived versus model-derived DTG (d).

For rosehip skin, lower TG error with increasing K did not produce a stable or thermally faithful representation. Global RMSE decreased from 2.693 percentage points for K = 1 to 1.713 for K = 2 and 1.412 for K = 3; mean withheld-rate RMSE decreased from 3.228 to 2.126 and 1.846 percentage points, respectively. However, K = 2 placed its second activation-energy center at the imposed upper bound, whereas K = 3 placed the third center and two pre-exponential factors at their imposed bounds. The comparatively stable K = 1 candidate reproduced the overall TG decline but retained heating-rate-dependent bias and terminal-mass overprediction (Fig. 8a). The model-derived DTG produced spurious onset spikes and did not reproduce the measured multistage derivative topology (Fig. 8b). The additional Gaussian domains therefore increased numerical flexibility without yielding stable reactivity modes or preserving the measured DTG architecture. Skin was consequently represented primarily by its measured multistage TG–DTG and isoconversional profiles, while the DAEM candidates were retained as model-adequacy diagnostics (Supplementary Tables S24–S28; Supplementary Figures S9–S12).

For whole-fruit rosehip, K = 3 gave the closest calibration to the three retained curves, with a global RMSE of 0.841 percentage points and rate-specific errors of 0.681, 0.678, and 1.095 percentage points at 5, 10, and 15 °C min^{-1}, respectively. These errors show that K = 3

reproduced the principal TG curvature across the three retained calibration conditions. The fitted trajectories followed the principal TG curvature of the three calibration curves (Fig. 8c), although signed residual structure remained, most prominently at 15 °C min^{-1} (Fig. 8d). Because the 20 °C min^{-1} curve was neither used for calibration nor evaluated as an independent prediction, the close three-curve fit does not establish transfer to an unseen heating condition. The fitted activation-energy centers were 128.5, 195.7, and 316.2 kJ mol^{-1}; the corresponding widths were 8.5, 12.7, and 54.3 kJ mol^{-1}, and the formal mass-loss capacities were 0.158, 0.311, and 0.213. Across near-optimal solutions, the spreads were 13.76 kJ mol^{-1} for center positions, 11.96 kJ mol^{-1} for distribution widths, and 0.81 log_{10} units for pre-exponential factors. The three ordered domains were therefore interpreted as empirical reactivity modes rather than constituent identities. Accordingly, K = 3 is reported as a three-rate calibration model, while independent predictive validation requires performance against data not used in parameter estimation [55] (Tables S24–S27; Figures S13–S15).

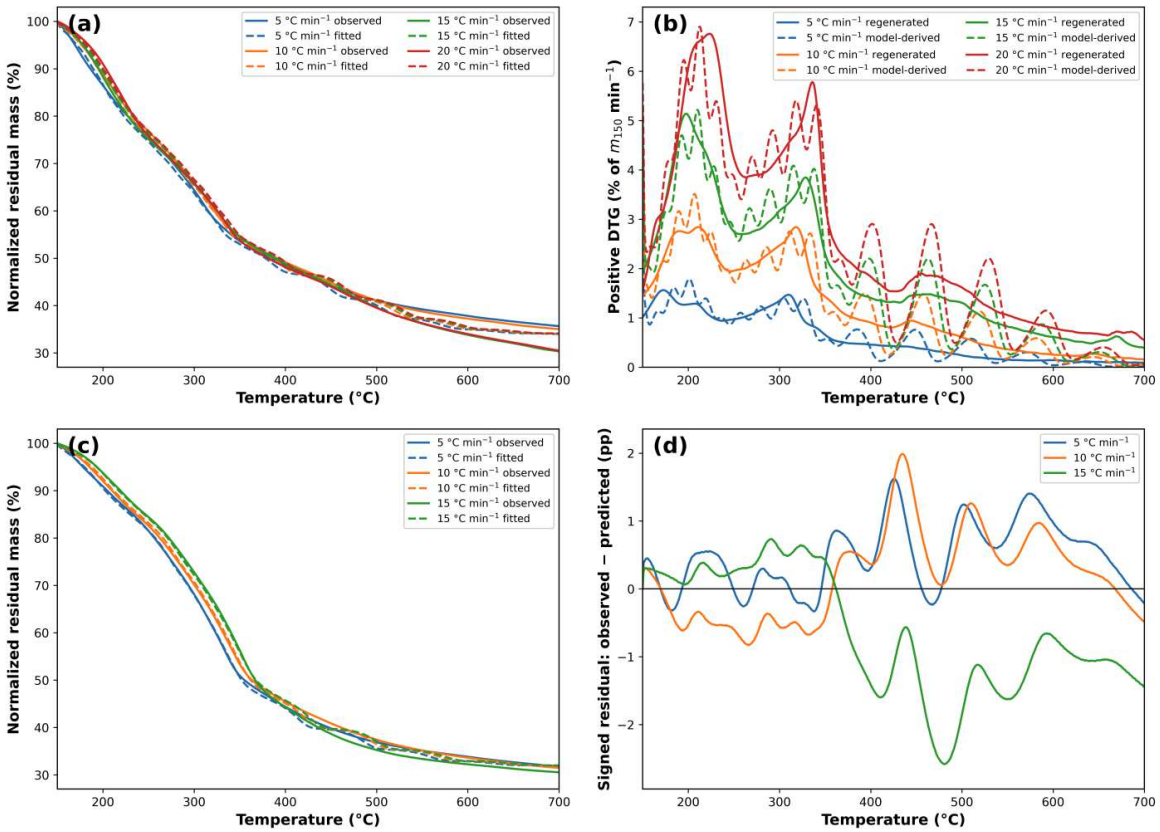


Fig. 8. Gaussian-DAEM adequacy diagnostics for rosehip skin (a,b) and whole-fruit rosehip (c,d). Panels (a,b) show skin TG calibration and derivative-shape mismatch; panels (c,d) show three-rate whole-fruit calibration and signed residuals.

Across the three preparations, DAEM performance depended on more than calibration error. Seed supported a compact K = 2 representation with partial cross-condition transfer; skin showed that lower error can coexist with unstable parameters and loss of derivative-shape fidelity; and whole fruit yielded a close K = 3 three-rate calibration without independent

prediction. The principal modelling outcome is that a low TG fitting error alone did not ensure stable parameters, prediction of an unfitted heating-rate curve, or reproduction of the measured DTG architecture. Accordingly, interpretation remained anchored to measured TG–DTG behaviour and analytical-support-screened isoconversional results, consistent with DAEM studies that assess model adequacy across broader thermal programmes and against data not used for parameter estimation [53,56,57].

3.3 Integrated interpretation of rosehip thermal responses

The combined evidence demonstrates that rosehip seed, skin, and whole fruit were not thermally interchangeable under the investigated TGA conditions. For each preparation, conversion timing and terminal mass retention, temperature-resolved mass-loss distribution, conversion-dependent apparent energy demand, and Gaussian-DAEM adequacy were interpreted together. This preparation-wise integration tests whether the descriptors converge on a coherent thermal-response architecture rather than restating each analytical section independently. Measured TG–DTG behaviour, recurring-domain architecture, and analytically supported $E_a(\alpha)$ trajectories provide the primary evidence, whereas Gaussian-DAEM performance provides secondary evidence concerning descriptive fit, parameter stability, derivative fidelity, and transfer across heating conditions [4,19,23]. Endpoint testing further showed that the preparation-specific trajectory directions and the shared-window ordering persisted across T_f = 600–700 °C, although absolute E_a magnitudes, particularly for skin, remained terminal-mass-dependent (Table 1; Supplementary Figure S16).

Seed entered conversion latest, with T_5% values of 180.3–228.0 °C. At 20 °C min^{-1}, T_{50}% was 368.3 °C and R_{700} was 22.91%. Its Stage II loss of 56.85% was the largest among the three preparations, and the single recurring DTG domain at 332–360 °C showed that this loss was concentrated within a comparatively narrow higher-temperature region. Consistent with this architecture, $E_a(\alpha)$ increased from 99.25 to 147.16 kJ mol^{-1} over α = 0.10–0.70 and then remained comparatively stable through the central conversion interval. The retained K = 2 DAEM reproduced the dominant multirate TG trend with partial cross-condition transfer, but its derivative mismatch limited it to a reduced-order descriptive representation. Seed therefore exhibits delayed access to a concentrated conversion region with a comparatively uniform mid-conversion apparent-energy requirement, while the DAEM should not be interpreted as a mechanistic decomposition (Supplementary Tables S2, S4, S13, S19–S22, and S24–S25).

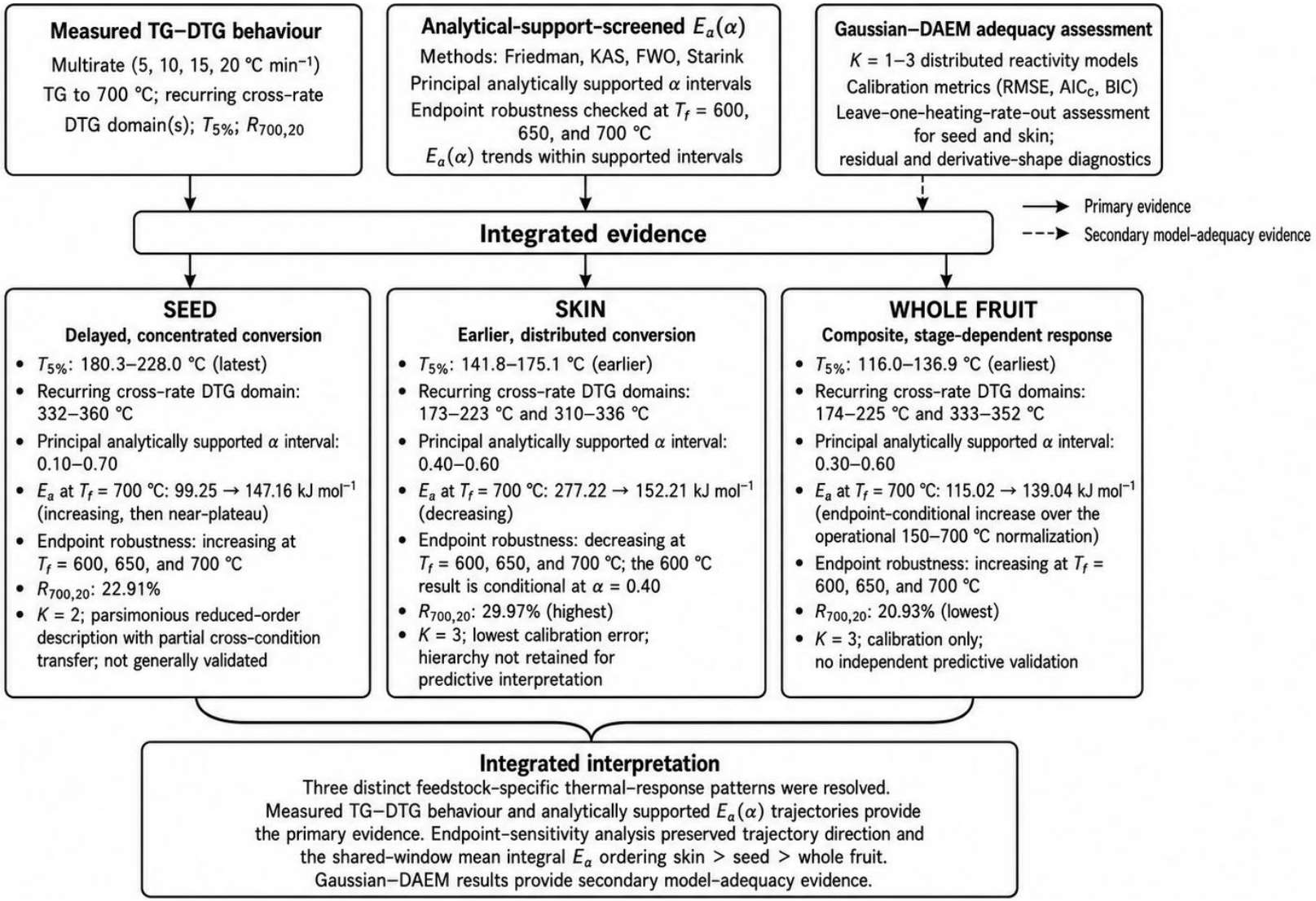


Fig. 9. Preparation-wise integration of conversion timing and terminal retention, mass-loss distribution, analytically supported Ea(α) trajectories, and Gaussian-DAEM adequacy for rosehip seed, skin, and whole fruit

Skin began conversion earlier, with $T_5\%$ values of 141.8–175.1 °C, yet at 20 °C min^{-1} it had the latest $T_{50}\%$ (372.3 °C) and the highest R_{700} (29.97%). Earlier onset therefore did not correspond to earlier progression through the central conversion region or lower terminal mass retention. Its Stage II loss was 50.95%, but this aggregate value was distributed between recurring domains at 173–223 and 310–336 °C, with the lower-temperature domain remaining dominant or co-dominant. The distributed multistage response was accompanied by the strongest conversion dependence in apparent energy demand: $E_a(\alpha)$ decreased from 277.22 to 152.21 kJ mol^{-1} over α = 0.40–0.60. Increasing Gaussian complexity lowered TG error, but it did not simultaneously yield stable parameters or reproduce the measured multistage DTG topology. Skin is therefore best characterized as an earlier, distributed conversion architecture with pronounced kinetic evolution and greater terminal retention, for which the measured TG–DTG and isoconversional results remain more informative than the DAEM candidates (Supplementary Tables S2, S4, S10–S13, S19–S22, and S24–S28).

Whole fruit showed the earliest low-conversion response, with $T_5\%$ values of 116.0–136.9 °C. At 20 °C min^{-1}, it also had the lowest $T_{50}\%$ (355.6 °C) and R_{700} (20.93%). Nevertheless, its Stage II loss of 53.27% lay between those of seed and skin, and its recurring domains at 174–225 and 333–352 °C were persistently dominated by the higher-temperature response. Thus, the earliest onset coexisted with sustained higher-temperature conversion. On the adopted endpoint-conditioned basis, $E_a(\alpha)$ increased from 115.02 to 139.04 kJ mol^{-1} over α = 0.30–0.60, indicating progressively greater effective apparent energy demand within the retained interval. The K = 3 model closely reproduced the three retained calibration curves, but its adequacy remained descriptive because transfer to an unseen heating condition was not established. Whole fruit therefore represents an independent integrated preparation characterized by early mass release and persistent higher-temperature-domain dominance, rather than a response that can be inferred through additive reconstruction of the separated fractions (Supplementary Tables S2, S4, S10–S12, S19–S22, and S24–S27).

Across the three preparations, the feedstock-wise integration resolves why no single descriptor provides a complete thermal ranking (Fig. 9). Similar Stage II losses did not imply equivalent conversion behaviour, because domain dominance, $E_a(\alpha)$ evolution, terminal mass retention, and model adequacy remained preparation-specific. Seed is defined by delayed and concentrated conversion, skin by earlier and distributed multistage conversion with the greatest terminal retention, and whole fruit by the earliest mass release coupled with sustained higher-temperature conversion. Recurring thermal domains and Gaussian reactivity modes remain operational and empirical descriptors, respectively, and were not assigned constituent identities. Preparation route is consequently a necessary analytical factor in rosehip thermal screening.

4. Conclusions

Under a common multirate TGA framework, rosehip seed, skin, and whole fruit exhibited distinct and non-interchangeable thermal-response architectures. Seed showed the latest low-conversion response and a comparatively concentrated higher-temperature conversion zone; skin converted earlier through two recurring domains and displayed the strongest conversion dependence in apparent energy demand; and whole fruit combined the earliest low-conversion mass loss with persistent dominance of the higher-temperature domain. The principal reliable $E_a(\alpha)$ conversion intervals were $\alpha = 0.10–0.70$ for seed, $\alpha = 0.40–0.60$ for skin, and $\alpha = 0.30–0.60$ for whole fruit. Endpoint-sensitivity analysis preserved the preparation-specific trajectory directions and the shared-window ordering skin > seed > whole fruit across $T_f = 600–700$ °C, although absolute E_a values remained terminal-mass-dependent, most strongly for skin. The 150–700 °C coordinate was retained as the primary basis, and the skin result at $T_f = 600$ °C and $\alpha = 0.40$ was classified as low-confidence. These results show that no single characteristic temperature, mean activation energy, or residue value adequately represents all three preparations; each requires interpretation through its own combination of conversion timing, domain structure, apparent-energy trajectory, and final mass retention.

Model evaluation further separated numerical fit from thermally meaningful representation. Recurring-domain analysis preserved the measured derivative structure more reliably than symmetric Gaussian DTG decomposition. For seed, the $K = 2$ DAEM provided a parsimonious reduced-order description with partial cross-condition transfer. For skin, lower calibration error with increasing model complexity did not yield stable parameters or reproduce the measured multistage derivative topology, so interpretation remained anchored to the measured TG–DTG and isoconversional results. For whole fruit, the $K = 3$ model provided the closest three-rate calibration but did not establish prediction at an unseen heating condition. The principal contribution is therefore an evidence-ranked framework that integrates measured TG–DTG behavior, recurring thermal-domain architecture, conversion-resolved apparent kinetics, and model-adequacy assessment. This framework provides a quantitative basis for preparation-specific thermal screening and for designing reactor studies that directly evaluate product yields, recovered-solid properties, and operating conditions.

Declarations

Ethics statement for the use of human and animal subjects

Not applicable. This study involved no human participants or animal experiments.

Competing Interest

The authors declare that they have no competing interests.

Author's Contribution

Ahsanullah Soomro: Conceptualization, Methodology, Investigation, Data curation, Formal analysis, Software, Visualization, Validation, Writing – original draft, Writing – review and editing,. **Anıl Tevfik Koçer:** Conceptualization, Methodology, Investigation, Validation, Formal analysis, Resources, Writing – review and editing. **Iqra Panhwar:** Data curation and Validation. **Zafar Ali Siyal:** Methodology and Validation. **Mahdi Hassan:** Formal analysis. **Hamid Rehman:** Data curation. **Tasawar Ali Chandio:** Visualization and Validation. **Didem Balkanlı:** Supervision, Resources, Validation, Writing – review and editing.

Availability of Data and Materials

All data supporting the findings of this study are available from the corresponding author upon reasonable request.

Acknowledgement

This project has received funding from the European Union's Horizon Europe research and innovation Program under the Marie Skłodowska-Curie grant Actions agreement No 101126655. The project is also partially supported in part by a research grant from the Scientific and Technological Research Council of Türkiye TÜBİTAK–ULAKBİM under the grant number 123C459.

Declaration of generative AI and AI-assisted technologies in the writing process.

During the preparation of this work the author(s) used several AI technologies in order to translate and provide the fluency of the writing. After using this tool/service, the author(s) reviewed and edited the content as needed and take(s) full responsibility for the content of the published article.

References

[1] A. Soomro, A.T. Koçer, D. Balkanlı, Biochar from food processing wastes: a multi-criteria roadmap for circular energy and environmental applications, Bioresources and Bioprocessing. 13 (2026) 80.
[2] C. Di Blasi, Modeling chemical and physical processes of wood and biomass pyrolysis, Progress in energy and combustion science. 34 (2008) 47-90.
[3] A.T. Koçer, A. Erarslan, A. Yurtseven, D. Balkanlı, Kinetic and biochar characteristics of lignocellulosic and protein-based industrial wastes during co-pyrolysis, Journal of Thermal Analysis and Calorimetry. (2026) 1-18.
[4] A. Anca-Couce, C. Tsekos, S. Retschitzegger, F. Zimbardi, A. Funke, S. Banks, T. Kraia, P. Marques, R. Scharler, W. de Jong, Biomass pyrolysis TGA assessment with an international round robin, Fuel. 276 (2020) 118002.
[5] A. Gani, I. Naruse, Effect of cellulose and lignin content on pyrolysis and combustion characteristics for several types of biomass, Renewable energy. 32 (2007) 649-661.
[6] L. Burhenne, J. Messmer, T. Aicher, M.-P. Laborie, The effect of the biomass components lignin, cellulose and hemicellulose on TGA and fixed bed pyrolysis, Journal of Analytical and Applied Pyrolysis. 101 (2013) 177-184.
[7] A. Soomro, A.T. Koçer, D. Balkanlı, Fraction-resolved pyrolysis behavior, conversion-dependent kinetics, and predictive severity framework for engineered biochars from fig-processing residues, Biomass and Bioenergy. 214 (2026) 109556.
[8] J.A. Conesa, A. Domene, Biomasses pyrolysis and combustion kinetics through n-th order parallel reactions, Thermochimica Acta. 523 (2011) 176-181.
[9] A. Skreiberg, Ø. Skreiberg, J. Sandquist, L. Sørum, TGA and macro-TGA characterisation of biomass fuels and fuel mixtures, Fuel. 90 (2011) 2182-2197.
[10] D.O. Usino, P. Ylitervo, A. Moreno, M.H. Sipponen, T. Richards, Primary interactions of biomass components during fast pyrolysis, Journal of Analytical and Applied Pyrolysis. 159 (2021) 105297.
[11] P.M. Ramos, J.M. Gil, M.C. Ramos Sánchez, L.M. Navas Gracia, S. Hernández Navarro, F.J. Martín Gil, Vibrational and thermal characterization of seeds, pulp, leaves and seed oil of Rosa rubiginosa, Boletín de la Sociedad Argentina de Botánica. 51 (2016) 429-439.
[12] R. Torres-Sciancalepore, D. Asensio, D. Nassini, A. Fernandez, R. Rodriguez, G. Fouga, G. Mazza, Assessment of the behavior of Rosa rubiginosa seed waste during slow pyrolysis process towards complete recovery: Kinetic modeling and product analysis, Energy Conversion and Management. 272 (2022) 116340.
[13] R. Torres-Sciancalepore, M. Riveros-Gomez, D. Zalazar-Garcia, D. Asensio, M.P. Fabani, R. Rodriguez, G. Fouga, G. Mazza, Two-step valorization of invasive species Rosa rubiginosa L. husk waste through eco-friendly optimized pectin extraction and subsequent pyrolysis, Journal of Environmental Chemical Engineering. 11 (2023) 110802.
[14] R. Torres-Sciancalepore, D. Nassini, D. Asensio, A. Bohé, R. Rodriguez, G. Fouga, G. Mazza, Synergistic effects of the mixing factor on the kinetics and products obtained by co-pyrolysis of Rosa rubiginosa rosehip seed and husk wastes, Energy Conversion and Management. 302 (2024) 118095.
[15] R. Torres-Sciancalepore, D. Zalazar-García, R. Rodriguez, G. Fouga, G. Mazza, Harnessing an Invasive Species' Waste for Syngas Production: Fast Pyrolysis of Rosehip Seeds in a Bubbling Fluidized Bed, ChemEngineering. 9 (2025) 146.
[16] E.B. Ates, D. Gunduz, Harnessing the energy potential of rosehip wastes towards sustainable energy supply, Process Safety and Environmental Protection. 187 (2024) 1481-1495.
[17] K. Slopiecka, P. Bartocci, F. Fantozzi, Thermogravimetric analysis and kinetic study of poplar wood pyrolysis, Applied Energy. 97 (2012) 491-497.
[18] A. Soomro, A.T. Koçer, M. Hassan, D. Balkanlı, Mechanism-resolved operating windows for biochar production from lavender distillation residue, Biochar. 8 (2026) 105.

[19] J. Cai, D. Xu, Z. Dong, X. Yu, Y. Yang, S.W. Banks, A.V. Bridgwater, Processing thermogravimetric analysis data for isoconversional kinetic analysis of lignocellulosic biomass pyrolysis: Case study of corn stalk, Renewable and Sustainable Energy Reviews. 82 (2018) 2705-2715.
[20] A.T. Koçer, B. İnan, B. Karacaoğlu, D. Balkanlı, M. Türker, Thermal decomposition behavior and kinetic analysis of microalgae from Lake Van (Türkiye): implications for biochar production, Reaction Kinetics, Mechanisms and Catalysis. (2026) 1-20.
[21] A. Soria-Verdugo, E. Goos, N. García-Hernando, Effect of the number of TGA curves employed on the biomass pyrolysis kinetics results obtained using the Distributed Activation Energy Model, Fuel Processing Technology. 134 (2015) 360-371.
[22] A. Koçer, D. Balkanlı, A thermal degradation study of disposable face mask wastes: determination of kinetic and thermodynamic parameters, International Journal of Environmental Science and Technology. 22 (2025) 5399-5410.
[23] G. Várhegyi, B. Bobály, E. Jakab, H. Chen, Thermogravimetric study of biomass pyrolysis kinetics. A distributed activation energy model with prediction tests, Energy & Fuels. 25 (2011) 24-32.
[24] V.I. Petkov, R. Joffe, P. Fernberg, Thermal oxidative aging of satin weave and thin-ply polyimide composites, Polymer Composites. 43 (2022) 2615-2627.
[25] A. Savitzky, M.J. Golay, Smoothing and differentiation of data by simplified least squares procedures, Analytical chemistry. 36 (1964) 1627-1639.
[26] S. Vyazovkin, A.K. Burnham, J.M. Criado, L.A. Pérez-Maqueda, C. Popescu, N. Sbirrazzuoli, ICTAC Kinetics Committee recommendations for performing kinetic computations on thermal analysis data, Thermochimica acta. 520 (2011) 1-19.
[27] M. Starink, The determination of activation energy from linear heating rate experiments: a comparison of the accuracy of isoconversion methods, Thermochimica acta. 404 (2003) 163-176.
[28] T. Akahira, T. Sunose, Method of determining activation deterioration constant of electrical insulating materials, Res Rep Chiba Inst Technol (Sci Technol). 16 (1971) 22-31.
[29] H.E. Kissinger, Reaction kinetics in differential thermal analysis, Analytical chemistry. 29 (1957) 1702-1706.
[30] J.H. Flynn, L.A. Wall, A quick, direct method for the determination of activation energy from thermogravimetric data, Journal of Polymer Science Part B: Polymer Letters. 4 (1966) 323-328.
[31] T. Ozawa, A new method of analyzing thermogravimetric data, Bulletin of the chemical society of Japan. 38 (1965) 1881-1886.
[32] M. Starink, A new method for the derivation of activation energies from experiments performed at constant heating rate, Thermochimica Acta. 288 (1996) 97-104.
[33] F. Motiee, S. Taghvaei-Ganjali, M. Malekzadeh, Investigation of correlation between rheological properties of rubber compounds based on natural rubber/styrene-butadiene rubber with their thermal behaviors, International Journal of Industrial Chemistry. 4 (2013) 16.
[34] S. Taghvaei-Ganjali, F. Motiee, F. Fotoohi, Correlation between physico-mechanical properties of NR-BR blends in tire tread formulation with their thermal behaviors, Rubber chemistry and technology. 81 (2008) 297-317.
[35] P. Mishra, C.M. Pandey, U. Singh, A. Gupta, C. Sahu, A. Keshri, Descriptive statistics and normality tests for statistical data, Annals of cardiac anaesthesia. 22 (2019) 67-72.
[36] L. Müller, G. Rubio-Pérez, A. Bach, N. Muñoz-Rujas, F. Aguilar, J. Worlitschek, Consistent DSC and TGA methodology as basis for the measurement and comparison of thermo-physical properties of phase change materials, Materials. 13 (2020) 4486.
[37] H.E. Kissinger, Variation of peak temperature with heating rate in differential thermal analysis, J. Res. Natl. Bur. Stand. 57 (1956) 217-221.
[38] S. Vyazovkin, Kissinger method in kinetics of materials: things to beware and be aware of, Molecules. 25 (2020) 2813.
[39] V. Singh, M. Musharraf, S. Swain, R. Dey, S. Shekhar, Thermal kinetics of poly (amidoamine) functionalized silica gel, (2023).
[40] K.P. Burnham, D.R. Anderson, Multimodel inference: understanding AIC and BIC in model selection, Sociological methods & research. 33 (2004) 261-304.

[41] T. Mani, P. Murugan, N. Mahinpey, Determination of distributed activation energy model kinetic parameters using simulated annealing optimization method for nonisothermal pyrolysis of lignin, Industrial & Engineering Chemistry Research. 48 (2009) 1464-1467.
[42] M. Isola, G. Colucci, A. Diana, A. Sin, A. Tonani, V. Maurino, Thermal properties and decomposition products of modified cotton fibers by TGA, DSC, and Py–GC/MS, Polymer Degradation and Stability. 228 (2024) 110937.
[43] L.L.R.L. de Castro, L.G. de Sousa Neiva, D.S.C. Andrade, Y.M.B. de Almeida, H. de Sousa E Silva, T.S. Alves, R. Barbosa, Sustainable Hybrid Films Based on Ecovio, Sodium Nitrite, and Babassu Mesocarp Starch for Potential Packaging Applications, Polymers for Advanced Technologies. 37 (2026) e70550.
[44] H. Wang, X. Yan, Q. Wang, W. Wu, Y. Tian, Q. Xu, Study on the Modification Mechanism and Rheological Properties of Bio-Oil-Based Composite-Modified Material for TOP-DOWN Crack Treatment in Long-Life Pavement, Journal of Composites Science. 10 (2026) 298.
[45] Y. Liu, L. Yang, C. Ma, Y. Zhang, Thermal behavior of sweet potato starch by non-isothermal thermogravimetric analysis, Materials. 12 (2019) 699.
[46] H. Yang, R. Yan, H. Chen, D.H. Lee, C. Zheng, Characteristics of hemicellulose, cellulose and lignin pyrolysis, Fuel. 86 (2007) 1781-1788.
[47] J.E. White, W.J. Catallo, B.L. Legendre, Biomass pyrolysis kinetics: a comparative critical review with relevant agricultural residue case studies, Journal of analytical and applied pyrolysis. 91 (2011) 1-33.
[48] J.M. Sanchez-Silva, R. Ocampo-Pérez, E. Padilla-Ortega, D. Sangaré, M.A. Escobedo-Bretado, J.L. Domínguez-Arvizu, B.C. Hernández-Majalca, J.M. Salinas-Gutiérrez, A. López-Ortiz, V. Collins-Martínez, Pyrolysis kinetics of Byrsonima crassifolia stone as agro-industrial waste through isoconversional models, Molecules. 28 (2023) 544.
[49] H. Mahmood, A. Shakeel, A. Abdullah, M.I. Khan, M. Moniruzzaman, A comparative study on suitability of model-free and model-fitting kinetic methods to non-isothermal degradation of lignocellulosic materials, Polymers. 13 (2021) 2504.
[50] A. Soria-Verdugo, M.T. Morgano, H. Mätzing, E. Goos, H. Leibold, D. Merz, U. Riedel, D. Stapf, Comparison of wood pyrolysis kinetic data derived from thermogravimetric experiments by model-fitting and model-free methods, Energy Conversion and Management. 212 (2020) 112818.
[51] O. Fischer, R. Lemaire, A. Bensakhria, Thermogravimetric analysis and kinetic modeling of the pyrolysis of different biomass types by means of model-fitting, model-free and network modeling approaches, Journal of Thermal Analysis and Calorimetry. 149 (2024) 10941-10963.
[52] J. Cai, W. Wu, R. Liu, An overview of distributed activation energy model and its application in the pyrolysis of lignocellulosic biomass, Renewable and Sustainable Energy Reviews. 36 (2014) 236-246.
[53] Z. Mercier, M. Carrier, F. Marias, Lumped and distributed activation energy modelling of biomass pyrolysis, Chemical Engineering Journal Advances. (2026) 100998.
[54] B. Xing, Y. Hu, H. Su, L. Wang, S. Wang, GCCo-Pyrolysis Behavior and Analysis of Synergistic Effects of Cellulose-Plastic Blends, Journal of Analytical and Applied Pyrolysis. (2026) 107941.
[55] A. Hodroj, N. Courtois, S. Delcour, D. Marquis, C. Brissot, P. Perré, A predictive multi-distribution activation energy modeling (DAEM) of the thermal behavior of model bituminized waste products (BWP) via thermogravimetry: A. Hodroj et al, Journal of Thermal Analysis and Calorimetry. (2026) 1-18.
[56] P. Perré, Y. Tian, P. Lu, B. Malinowska, J. El Bekri, J. Colin, A robust and frugal model of biomass pyrolysis in the range 100–800° C: Inverse analysis of DAEM parameters, validation on static tests and determination of heats of reaction, Fuel. 288 (2021) 119692.
[57] J. Pallarés Ranz, C.b. Cortés, A. Gil, I. Arauzo, Kinetic Characterization of Barley Straw Carbonization Using the Distributed Activation Energy Model (DAEM), ACS Omega. (2026).

Supplementary Files

This is a list of supplementary files associated with this preprint. Click to download.

- suplementaryfile.docx